JEM Journal of Experimental Medicine

ARTICLE

NIK-driven IL-23 production by myeloid cells is a key factor in the development of autoimmune inflammation

Nishada S. Ramphal[1], Xinyuan Liu[1], Ilaria Palagi[1], Rebecca Jasser[1], Alma N. Mohebiany[1], Matthias Klein[4], Frederike Westermann[2], Sinduya Krishnarajah[2], Tommy Regen[1,3], Tobias Bopp[3,4], Burkhard Becher[2], and Ari Waisman[1,3]

NIK (*Map3k14*) is a central regulator of noncanonical NF-κB signaling and immune homeostasis. Mutations in this kinase are linked to autoimmune disorders, including multiple sclerosis (MS). Both germline and T cell–specific deletion of NIK had been demonstrated previously to be associated with resistance to developing experimental autoimmune encephalomyelitis (EAE), an animal model for MS. In this study, we show that NIK expression by circulating myeloid cells is crucial for EAE development. Mechanistically, we found starkly reduced priming of neuroantigen-specific T cells in the absence of NIK in CX3CR1$^+$ cells. This reduction was associated with dysregulated expression of genes involved in antigen presentation and cell migration, as well as decreased IL-23 production. Notably, T cells primed by NIK-deficient myeloid cells regained their ability to induce EAE when incubated with IL-23 before being transferred into Rag^{KO} mice. Our data underline the crucial role of NIK in enabling myeloid cells to function effectively as antigen-presenting cells.

Introduction

The noncanonical NF-κB signaling pathway regulates many aspects of the immune and stress response (Sun and Ley, 2008; Pflug and Sitcheran, 2020). This pathway can be activated via receptors that are part of the tumor necrosis factor superfamily, including lymphotoxin β receptor, B cell–activating factor receptor, receptor activator of NF-κB, Tweak receptor, CD40, and CD27 (Sun, 2012; Sun, 2017). The primary stimulator of this pathway is NF-κB–inducing kinase (NIK), also termed mitogen-activated protein kinase kinase kinase 14 (MAP3K14) (Sun and Ley, 2008). During steady state, NIK is bound to tumor necrosis factor receptor–associated factor 3 (TRAF3), which results in the degradation of NIK by the proteasome. Activation of the pathway by inflammatory mediators induces the degradation of TRAF3, leading to the stabilization and accumulation of NIK (Liao et al., 2004). This results in NIK phosphorylating its downstream target, IκB-specific kinase α, which subsequently induces the activation and translocation of the p52-RelB complex, resulting in the transcription of multiple genes involved in immune response and inflammation (Shih et al., 2015; Xiao et al., 2001).

In humans, mutations in the NIK (*MAP3K14*) gene are linked to immunodeficiencies and result in various clinical manifestations like lymphopenia, impaired B cell survival, and defects in follicular helper/memory T cell populations and natural killer cells (Schlechter et al., 2017; Willmann et al., 2014; Pflug and Sitcheran, 2020). Notably, NIK has been identified as a susceptibility gene for conditions such as rheumatoid arthritis and multiple sclerosis (MS) (Hussman et al., 2016; Pflug and Sitcheran, 2020; Schlechter et al., 2017). Also in mice, it has been demonstrated that strains without functional NIK are immunodeficient and lack secondary lymphoid organs (Miyawaki et al., 1994). These mice, known as NIK$^{aly/aly}$ mice, exhibit severe immune deficiency; however, this is unrelated to the absence of secondary lymphoid tissues (Greter et al., 2009). Even mice lacking all lymph nodes (LNs) and spleen will develop fulminant experimental autoimmune encephalomyelitis (EAE) upon immunization if NIK signaling is restored across leukocytes (Hofmann et al., 2011; Jin et al., 2009).

Further studies have established NIK as a crucial regulator in the development of B cells, specific macrophage (Mac) subsets, and an intrinsic mediator of T cell function in immune and autoimmune responses (Brightbill et al., 2018; Hahn et al., 2016; Hamdan et al., 2020; Lacher et al., 2018). Additionally, NIK is described to play a critical role in intestinal homeostasis and psoriasis-like skin disease in mice (Huang et al., 2018; Jie et al.,

[1]Institute for Molecular Medicine, University Medical Center of the Johannes Gutenberg University Mainz, Mainz, Germany; [2]Institute of Experimental Immunology, University of Zurich, Zurich, Switzerland; [3]Research Center for Immunotherapy (FZI), University Medical Center of the Johannes Gutenberg University of Mainz, Germany; [4]Institute for Immunology, University Medical Center of the Johannes Gutenberg, University Mainz, Mainz, Germany.

Correspondence to Ari Waisman: waisman@uni-mainz.de.

© 2026 Ramphal et al. This article is distributed under the terms as described at https://rupress.org/pages/terms102024/.

Check for updates

Downloaded from http://rupress.org/jem/article-pdf/223/4/e20242294/2027553/jem_20242294.pdf by guest on 31 May 2026

2018). However, the role of NIK in dendritic cells (DCs) during EAE remains less clear. Studies have shown that the accumulation of NIK in DCs can exacerbate EAE, leading to increased CNS infiltration by immune cells and a higher number of T_H17 cells (Huang et al., 2018). Using the $NIK^{aly/aly}$ mice, it was also demonstrated that NIK in DCs is critical for effector T cell function and the progression of EAE (Hofmann et al., 2011). In contrast, others suggested that the cell-specific deletion of NIK in DCs does not alter $CD4^+$ T cell priming or EAE development, indicating that the role of NIK in DCs is controversial and may be more complex than initially understood (Katakam et al., 2015).

Monocytes are as abundant as DCs in the LNs, and during inflammation, they outnumber the LN-resident myeloid cells. They can differentiate into monocyte-derived macrophages (MoMacs) and DCs (moDCs) (Amorim et al., 2022), act as antigen-presenting cells (APCs), and prime both CD8 and CD4 T cells (Jakubzick et al., 2017). Elevated numbers of inflammatory monocytes have been reported in the blood of NIK^{KO} mice compared with control mice (Keeney et al., 2023). However, the role of the noncanonical NF-κB pathway and NIK in monocytes and their progeny, hereafter called monocyte-derived cells, during autoimmune inflammation is poorly understood. Furthermore, while NIK is a known regulator of IL-23 in skin and intestinal inflammation, its role in CNS autoimmunity remains poorly defined. Specifically, it remains to be determined whether NIK is required to program circulating myeloid cells with the necessary transcriptional profile to present antigen during the induction of CNS autoimmunity. We therefore investigated the role of NIK in phagocytes within the context of the EAE model by generating $NIK^{\Delta CX3CR1}$ mice, as CX3CR1 is expressed across various myeloid cell populations, including microglia, monocytes, and cDCs (Yona et al., 2013; Jung et al., 2000). Our findings reveal that NIK signaling in peripheral CX3CR1-expressing cells is pivotal for EAE susceptibility, shaping both antigen presentation and the production of pro-encephalitogenic cytokines, such as IL-23. Of note, while $NIK^{\Delta CX3CR1}$ mice were protected from EAE, deletion of NIK only in microglia did not confer protection, highlighting the importance of peripheral myeloid cells. These results underline the key role of NIK in regulating immune responses critical for EAE progression.

Results

NIK signaling across the mononuclear phagocyte system plays a critical role in the development of EAE

To study the role of NIK in myeloid cells, we crossed the $NIK^{fl/fl}$ to the CX3CR1-Cre (Yona et al., 2013), which efficiently targets multiple myeloid populations, including Macs, monocytes, and cDC2s. Using an RFP reporter, we confirmed that this model efficiently targets these myeloid populations, with minimal targeting of T or B cells at 5 days after MOG immunization (Fig. S1 A). We found that these $NIK^{\Delta CX3CR1}$ mice were completely resistant to EAE induction (Fig. 1, A and B). Accordingly, we found minimal numbers of infiltrating immune cells in the CNS during the peak of the disease (Fig. 1 C). This included a decrease in the number and percentage of neutrophils ($CD45^{high}$ $CD11b^+$ $Ly6G^+Ly6C^+$) and monocytes ($CD45^{high}$ $CD11b^+$ $Ly6C^{high}$) (Fig. S1, C–E). Additionally, we observed a significant reduction in CNS-infiltrating $CD4^+$ T cells and almost none of these were MOG-specific $CD44^+CD40L^+$ T cells, nor did they produce IL-17A, GM-CSF, or IFNγ (Fig. 1, D–F). Analysis of the peripheral organs following EAE induction revealed no significant differences in the number and percentage of neutrophils, monocytes, and $CD4^+$ T cells in the spleen and the skin-draining lymph nodes (dLN) during the peak of disease (Fig. 1 G and Fig. S1, C–E). However, fewer MOG-specific T cells, including cytokine-producing T cells, were observed in the dLN and spleens of $NIK^{\Delta CX3CR1}$ mice during the peak of the disease (Fig. 1, H and I). Previous studies have shown a strong link between the commensal bacterial composition of the gut and the ability to raise encephalitogenic T cells (Brockmann et al., 2023; Regen et al., 2021). To determine whether the loss of NIK would have a significant influence on the gut microbial composition, we compared the steady-state gut microbiome between genotypes. The Shannon diversity, β-diversity (PCoA), and the relative abundance of dominant taxa were comparable, indicating no baseline microbiota differences (Fig. S1, F–H).

CX3CR1-Cre targets various myeloid populations, including Macs, cDC2s, and moDCs (Jung et al., 2000). The role of NIK signaling in DCs is a matter of debate: while there are strong data suggesting that NIK engagement in DCs is vital for their priming capacity (Hofmann et al., 2011), others found that the deletion of NIK in DCs using CD11c-Cre mice does not affect the course of EAE (Katakam et al., 2015). The latter data would suggest that the resistance to EAE observed in our $NIK^{\Delta CX3CR1}$ mice is likely due to NIK deficiency in $CX3CR1^+CD11c^-$ cells. To further validate that the loss of NIK signaling can lesion the myeloid compartment, we crossed our $NIK^{fl/fl}$ mice with the CD11c-Cre ($NIK^{\Delta CD11c}$), which targets mainly cDC populations and some Macs in the LNs. This was confirmed by RFP reporter analysis at the onset of disease (5 days after immunization [dpi]), which showed robust RFP expression across the relevant myeloid subsets (Fig. S1 B). In agreement with Hofmann et al., but in contrast to Katakam et al. our $NIK^{\Delta CD11c}$ mice were highly resistant to develop EAE, phenocopying the $NIK^{\Delta CX3CR1}$ mice (Fig. 1, J and K).

Microglia are also targeted by the CX3CR1-Cre. Therefore, to specifically test the role of NIK in microglia during EAE, we crossed the $NIK^{fl/fl}$ mice to the tamoxifen-inducible $CX3CR1\text{-}Cre^{ERT2}$ mice (Wolf et al., 2013; Yona et al., 2013), resulting in the $NIK^{\Delta MG}$ mice. Following treatment with tamoxifen, short-lived myeloid cells such as monocytes are replaced by newcomers from the bone marrow, leaving long-lived cells such as border-associated macrophages (BAMs) and microglia deficient for NIK. To confirm efficient deletion of NIK (*Map3k14*) in microglia, qPCR was performed on MACS-purified microglia isolated 10 weeks after tamoxifen induction. Primers spanning the floxed exons of *Map3k14* revealed a strong reduction of the targeted exon in $NIK^{\Delta MG}$ mice compared with controls, validating effective recombination in microglia (Fig. S2 A). We found that the $NIK^{\Delta MG}$ mice were fully susceptible to EAE, with no significant differences in the disease score or the number of infiltrating cells into the CNS during the peak of EAE compared with controls (Fig. S2, B–E). Furthermore, no differences were observed in the MFI of various activation markers on microglia, in

Downloaded from http://rupress.org/jem/article-pdf/223/4/e20242294/2027553/jem_20242294.pdf by guest on 31 May 2026

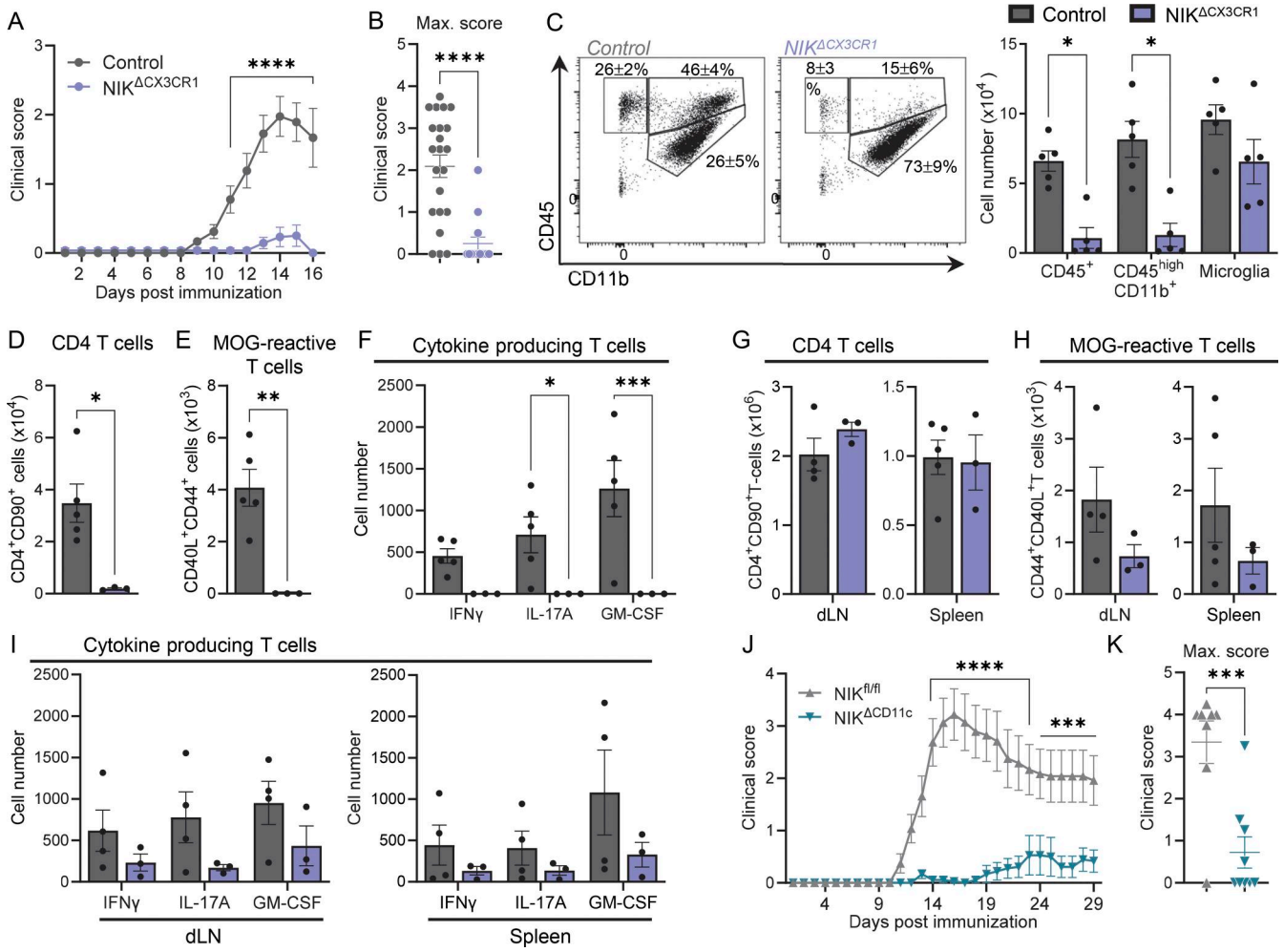

Figure 1. **NIK in CX3CR1-expressing cells drives EAE pathology. (A)** Disease course of NIK$^{\Delta CX3CR1}$ and littermate controls. **(B)** Maximum EAE score. Data in A and B are the cumulative data of 3 individual experiments. **(C)** Representative flow cytometry plots with mean percentages ±SEM, and the number of microglia (CD11b^{+}CD45^{int}), infiltrating CD45^{high} and CD11b^{+}CD45^{high} immune cells into the CNS during the peak of EAE (15 dpi). **(D–F)** Number of CD4^{+}CD90^{+} T cells, (E) MOG-responding cells (CD40L^{+}CD44^{+}), (F) and IL-17A, IFNγ, or GM-CSF by these T cells after a 6-h MOG_{35-55} antigen recall assay in the CNS (brain and spinal cord). **(G–I)** Number of CD4^{+}CD90^{+} T cells, (H) MOG-responding cells (CD40L^{+}CD44^{+}), (I) and IL-17A, IFNγ, or GM-CSF by these T cells after a 6-h MOG_{35-55} antigen recall assay in the dLN and spleen. Duplets and dead cells were excluded before gating on shown cell populations. **(J and K)** EAE disease development and (K) maximum EAE score in NIK$^{\Delta CD11c}$ mice and littermate controls. Data are shown as the mean ± SEM and analyzed using two-tailed unpaired Student's *t* test or two-way ANOVA with Šídák's multiple comparisons test. *P < 0.05, **P < 0.01, ***P < 0.001, ****P < 0.0001. Each dot represents one mouse. Data (C–K) are from at least two independent experiments. dpi = days after immunization. dLN = draining lymph nodes.

the proportions of MOG-reactive T cells, and different T cell subsets in the CNS of NIK$^{\Delta MG}$ mice and controls (Fig. S2, F and G). These findings indicate that NIK signaling within the CNS-resident microglia and BAM compartment does not affect the development of EAE or the infiltration of T cell subsets during the peak of EAE.

Taken together, NIK signaling in mononuclear myeloid cells including MoMacs and cDCs is vital for the generation of an encephalitogenic autoimmune response, whereas NIK engagement in microglia and BAMs is not involved in the pathogenesis of EAE.

Impaired T cell priming in the secondary lymphoid organs of NIK$^{\Delta CX3CR1}$

Our data show that the NIK expression in systemic mononuclear myeloid cells is critical for the induction of EAE. However, whether this is due to the inability of APCs to activate pathogenic T cells or the absence of NIK leading to an overall tolerogenic environment in the mice needs to be evaluated. To test this, we isolated encephalitogenic wild-type T cells from spleens and LN of MOG-immunized mice after 8 days and transferred them to NIK$^{\Delta CX3CR1}$ and littermate control mice (Fig. 2 A). We found that the transferred encephalitogenic T cells were able to induce similar disease in both NIK$^{\Delta CX3CR1}$ and control mice (Fig. 2, B and C). These findings indicate that insufficient T cell priming by APCs is most likely to be responsible for the lack of EAE development in the NIK$^{\Delta CX3CR1}$ mice.

To test this, we immunized NIK$^{\Delta CX3CR1}$ and littermate control mice and isolated cells from the spleen and dLN 8 dpi, before disease onset (Fig. 2 D). After *ex vivo* restimulation of the cells with MOG, we noticed a reduction in the number of CD4^{+} T cells in the dLNs (Fig. 2 E), associated with a decrease in MOG-reactive T cells

Downloaded from http://rupress.org/jem/article-pdf/223/4/e20242294/2027553/jem_20242294.pdf by guest on 31 May 2026

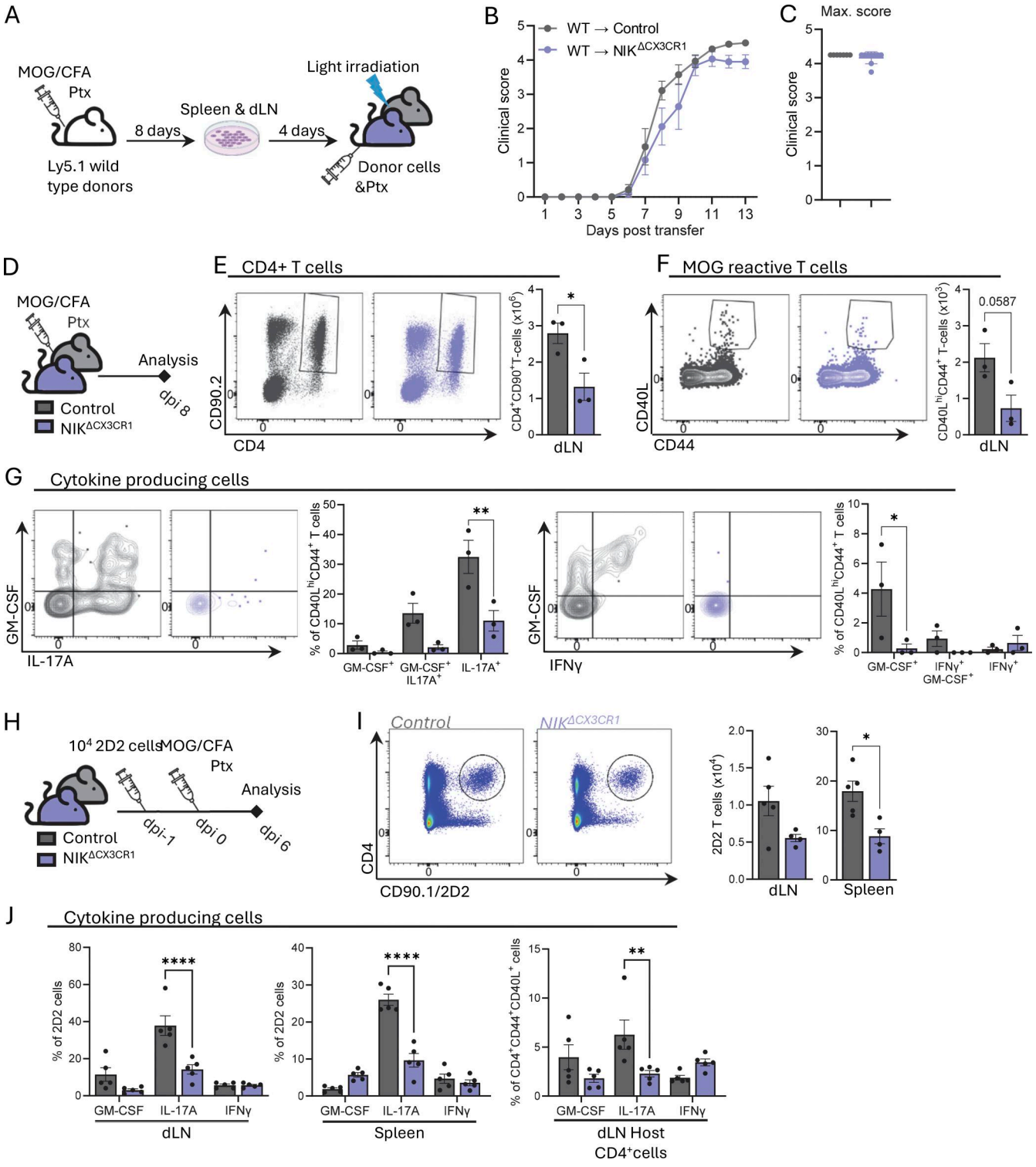

Figure 2. **Less cytokine-producing T cells in secondary lymphoid organs before EAE onset. (A)** Scheme of the adoptive transfer EAE model: Ly5.1 wild-type mice were immunized with MOG_{35-55}/CFA and PTx; isolated cells from dLNs and spleen were cultured for 4 days with MOG_{35-55}, IL-23, and anti-IFNγ before being injected into $NIK^{\Delta CX3CR1}$ and littermate controls. **(B and C)** Passive transfer EAE disease course and (C) maximum EAE score of $NIK^{\Delta CX3CR1}$ and littermate controls after adoptive transfer of MOG-activated wild-type T cells. **(D–F)** Experimental scheme: $NIK^{\Delta CX3CR1}$ and littermate control mice were immunized with MOG_{35-55}/CFA and PTx, and cells were isolated from the spleen and dLN at 8 dpi and restimulated with MOG for 6 h. **(E)** Representative flow cytometry plots and total cell number of $CD4^+CD90^+$ T cells and (F) MOG-reactive ($CD44^+CD40L^+$) T cells. **(G)** Representative flow cytometry plots and percentages of IL-17A, GM-CSF, and IFNγ-producing T cells. **(H and I)** 2D2 T cells were transferred into $NIK^{\Delta CX3CR1}$ and littermate controls 1 day before MOG_{35-55} immunization. Six dpi, cells were isolated from the spleen and dLN and re-stimulated with PMA, ionomycin, and brefeldin A. **(I)** Representative flow cytometry plots of the spleen and the total cell number of transferred $CD90.1^+CD4^+$ 2D2 cells. **(J)** Percentages of 2D2 T cells that produce IL-17A, GM-CSF, or IFNγ in the dLNs and spleen and cytokine-producing $CD4^+$ host cells, pregated on live/single cells. Data in graphs are shown as the mean ± SEM and analyzed using two-tailed unpaired Student's *t* test or two-way ANOVA with Šídák's multiple comparisons test. *P < 0.05, **P < 0.01, ****P < 0.0001. Each dot represents one mouse. Data are from at least three independent experiments. dpi = days after immunization.

Downloaded from http://rupress.org/jem/article-pdf/223/4/e20242294/2027553/jem_20242294.pdf by guest on 31 May 2026

(Fig. 2 F). Additionally, the MOG-reactive T cells produced less IL-17A, GM-CSF, and IFNγ in the dLN of the NIK$^{\Delta CX3CR1}$ mice when compared to littermate controls (Fig. 2 G). Our findings indicate that NIK$^{\Delta CX3CR1}$ mice produce fewer encephalitogenic T cells during the priming phase of EAE, which likely contributes to their resistance to the disease.

To further strengthen this point, we transferred TcR transgenic 2D2 cells (which express a MOG-specific T cell receptor) into NIK$^{\Delta CX3CR1}$ mice and littermate controls. The mice were immunized with MOG/CFA 1 day later, and cells were isolated from the dLN and spleen 6 dpi (Fig. 2 H). The congenic marker CD90.1 allowed us to distinguish 2D2 cells from CD90.2$^+$ host cells. Significantly fewer 2D2 cells were observed in the spleen of NIK$^{\Delta CX3CR1}$ mice 6 days after MOG immunization, and a similar trend was observed in the dLNs (Fig. 2 I). Isolated cells from the spleen and dLN were restimulated with PMA and ionomycin *ex vivo* to investigate their cytokine production. Although no significant differences were observed in the production of IFNγ and GM-CSF, there was a significant reduction in IL-17A–producing 2D2 T cells in both the spleen and dLNs of the NIK$^{\Delta CX3CR1}$ mice (Fig. 2 J). Additionally, the same reduction of IL-17A–producing cells could be seen in the host cells of the NIK$^{\Delta CX3CR1}$ mice (Fig. 2 J). These data suggest that the deletion of NIK in CX3CR1-expressing cells impairs the differentiation of encephalitogenic T_H17s during the priming phase of EAE.

Previously, it was demonstrated that RelB, which functions downstream of NIK in the noncanonical NF-κB pathway, plays a crucial role in CD11c cells by regulating T_{reg} cell numbers. This regulation, in turn, protects against the development of EAE (Andreas et al., 2019). We examined whether T_{reg} cells could contribute to the EAE resistance observed in NIK$^{\Delta CX3CR1}$ mice. However, our data revealed no significant differences in the proportion of T_{reg} cells among all CD4$^+$ T cells in the spleen and dLNs at either 3 or 8 days post-MOG immunization (Fig. S3, A–C). Similarly, the percentage of T_{reg} cells in the CNS, spleen, and dLNs during the peak of EAE (15 dpi) was comparable between both groups (Fig. S3 D).

Taken together, our data show that while NIK in CX3CR1-expressing cells is crucial for regulating effector T cell function during the priming stage in EAE, it does not seem to affect the frequency of T_{reg} cells during EAE.

The myeloid compartment of NIK$^{\Delta CX3CR1}$ mice shows dysregulation of antigen presentation–associated genes

Using BD Rhapsody single-cell RNA sequencing (scRNA-seq), we obtained deeper insights into how the deletion of NIK in CX3CR1-expressing cells may affect T cell priming and result in EAE resistance. At 4 dpi, we isolated cells from the dLN of the NIK$^{\Delta CX3CR1}$ and control animals and enriched for myeloid cells by depleting most of the B and T cells. We then sequenced a total of 22,238 cells, however, clusters identified as contaminating lymphoid cells, pDCs, and neutrophils were excluded during initial analysis. Following this, we conducted unsupervised clustering on the remaining myeloid clusters. The resulting Uniform Manifold Approximation and Projection (UMAP) revealed a total of nine distinct myeloid cell clusters (Fig. 3 A). These clusters were further characterized based on their marker genes and annotated with the assistance of ImmGen and known literature (Fig. 3 B and Fig. S4 A). We identified three monocyte clusters: Ly6C^{hi} Mono (*Fn1*, *F13a1*, and *Vcan*), Ly6C^{lo} Mono (*Ear2*, *Ace*, and *Cd300e*), and a third monocyte population expressing *Cxcl10*, *Ifit3*, and *Ifit2*, which has been described to play a pathogenic role in EAE (Giladi et al., 2020) and was annotated as Cxcl10 Mono. Furthermore, a Mac cluster was identified with ImmGen based on the top 10 marker expressions (including *Mmp14*, *Clec4n*, and *Ffar2*). Notably, this cluster also shared some markers, like *Ly6c2* and *Ccr2*, with monocytes (Fig. 3 A and Fig. S4 A). Another cluster sharing both Mac markers and monocyte markers is the MoMac cluster (*C1qa*, *Mertk*, *C1qb*); a similar MoMac cluster has been described previously in the context of EAE (Amorim et al., 2022). In addition, we could identify four DC clusters, which all expressed *Flt3* (Fig. S4 A). These clusters were annotated as cDC1s (*Xcr1*, *Clec9a*, *Notch4*), cDC2s (*Cd209a*, *H2-Ob*, *Cd7*), migDCs (*Ccr7*, *Ly75*, *Ccl22*), and SiglecH$^+$ DCs (*Siglech*, *Nrgn*, *Il18r*) (Fig. 3, A and B; and Fig. S4 A). The latter resemble a murine Siglech$^+$ DC phenotype described by others and are believed to be transitional DCs in the process of transitioning from pre-DC to DC (Leylek et al., 2019; Lukowski et al., 2021).

Comparing the abundance of the myeloid population in dLN of NIK$^{\Delta CX3CR1}$ and control mice, we observed a rise in Ly6C^{lo} Mono and a decline in the Macs and cDC2 populations in NIK$^{\Delta CX3CR1}$ mice (Fig. 3, A and C). Furthermore, projecting a cell signature for antigen presentation (Amorim et al., 2022) on the myeloid cell subsets, we detected the highest score for antigen presentation within the Macs and DC clusters, which are decreased in NIK$^{\Delta CX3CR1}$ mice (Fig. 3 D and Fig. S4 B). These observations show that the NIK$^{\Delta CX3CR1}$ mice have a decrease in myeloid cells with the strongest antigen presentation potential 4 days after MOG immunization, which could explain the decrease in MOG-reactive T cells and the ameliorated EAE in these mice. Concurrently, we observed an increase of Ly6C^{lo} monocytes, which are usually found in the vasculature, where they patrol and play a role in tissue repair. However, whether these cells have any role in EAE disease development is yet unknown.

We employed the Milo package in R to analyze the variances in the mRNA level between control and NIK$^{\Delta CX3CR1}$ myeloid cells (Dann et al., 2022). Milo is a scalable statistical framework that assigns cells to partially overlapping small neighborhoods on a k-nearest neighbor graph and performs differential abundance testing. Through this approach, we were able to identify cell types exhibiting significant variances in abundance between our groups. Cells from our samples were assigned to 536 neighborhoods, with 96 of these showing differential abundance across multiple cell populations (Fig. 3 E). Most differentially abundant neighborhoods were found within the migDC, Ly6C^{lo} monocytes, Macs, and cDC2 populations (Fig. 3 F), meaning that within these clusters, cells might shift to a different activation state between the control and NIK$^{\Delta CX3CR1}$ mice after MOG immunization.

To gain further insight into the biological implications of the observed differences in cell abundance, we conducted an in-depth analysis, comparing between the different myeloid populations of control and NIK$^{\Delta CX3CR1}$ mice. This revealed numerous differentially expressed genes (DEGs) across several clusters (Table S1), indicating transcriptional differences associated

Downloaded from http://rupress.org/jem/article-pdf/223/4/e20242294/2027553/jem_20242294.pdf by guest on 31 May 2026

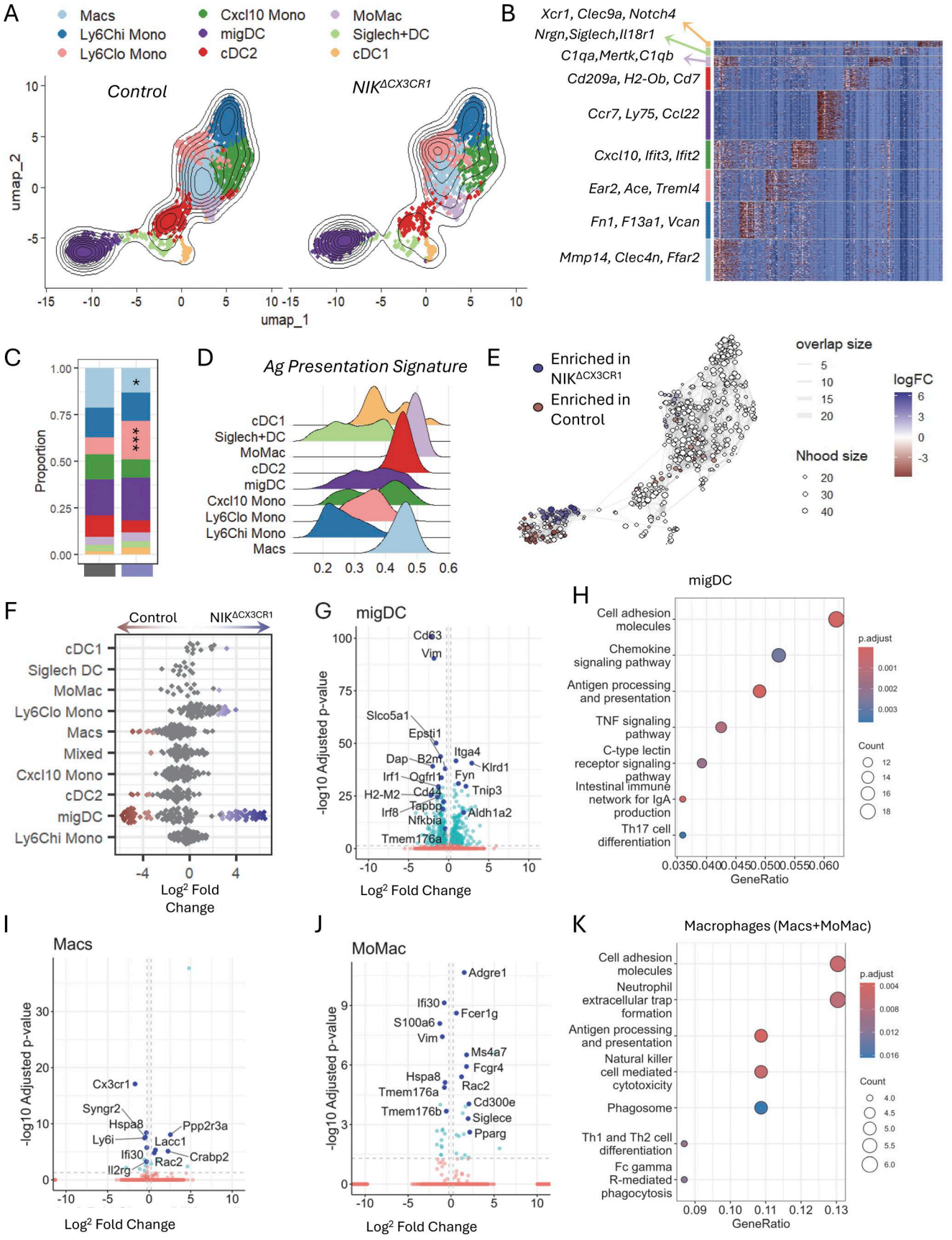

Figure 3. **scRNA-seq reveals dysregulation of antigen-presenting genes 4 days after MOG immunization in the dLNs. (A)** Density plots overlaid on the UMAP of control (n = 4) and NIK$^{\Delta CX3CR1}$ (n = 4) displaying clustering of myeloid cell type, excluding B, T, NK, and mast cells, pDCs, neutrophils, and granulocytes.

Downloaded from http://rupress.org/jem/article-pdf/223/4/e20242294/2027553/jem_20242294.pdf by guest on 31 May 2026

(B) Heatmap displaying the top 10 highly expressed markers of each cluster in A with three of the top markers per cluster written out. **(C)** Proportions of each cell type within the UMAP of the control (n = 4) and NIK$^{\Delta CX3CR1}$ (n = 4). **(D)** Antigen presentation cell signature score projected in each cluster, calculated with UCell. **(E)** 536 neighborhoods assigned by the Milo package overlaid on our UMAP of myeloid cell clusters. **(F)** Abundant neighborhoods across the different myeloid clusters. Red = more abundant in control, blue = more abundant in NIK$^{\Delta CX3CR1}$, FDR = 10%. **(G)** Volcano plot of DEGs between NIK$^{\Delta CX3CR1}$ and control in the migDC subset. Left is downregulated in NIK$^{\Delta CX3CR1}$, and right is upregulated in NIK$^{\Delta CX3CR1}$. **(H)** KEGG pathway enrichment analysis was performed on DEGs (adjusted P < 0.05 and |$\log_2$ fold change| >0.1 and <0.1) from the migDC clusters. **(I and J)** Volcano plot of DEGs between NIK$^{\Delta CX3CR1}$ and control in the Mac subset and (J) MoMac subset. Left is downregulated in NIK$^{\Delta CX3CR1}$, and right is upregulated in NIK$^{\Delta CX3CR1}$. **(K)** KEGG pathway enrichment analysis was performed on DEGs (adjusted P < 0.05 and |$\log_2$ fold change| >0.1 and <0.1) from the Mac clusters (Macs/MoMacs).The dot plot shows enriched pathways ranked by significance. Circle size = count of DEGs found within each pathway; color = adjusted P value. Data in C are shown as mean percentage and analyzed using two-way ANOVA with Šídák's multiple comparisons test. *P < 0.05, ***P < 0.001.

with NIK loss. Notably, the cDC1 and SiglecH$^+$ DC clusters did not display any significant DEGs (adjusted P <0.05).

Among all populations, migDCs exhibited the highest number of DEGs (Fig. 3 G), which was consistent with the Milo analysis, where most differentially abundant neighborhoods were found within the migDC cluster. Genes involved in antigen processing and presentation (*B2m*, *Tapbp*, *H2-M2*, *Cd63*), NF-κB and interferon signaling (*Irf1*, *Irf8*, *Nfkbia*), and cell adhesion and migration (*Cd44*) were reduced in NIK-deficient migDCs, indicating impaired activation and antigen presentation capacity. Correspondingly, KEGG pathway enrichment analysis of the DEGs using clusterProfiler revealed significant enrichment for pathways associated with antigen processing and presentation, chemokine and TNF signaling, and cell adhesion molecules (Fig. 3 H).

Within the resDC2 cluster, DEGs included *Cd300e*, *Pou2f2*, *Ifi30*, and *Hspa8* (Fig. S4 C). Although these changes did not result in significant KEGG pathway enrichment, several of these genes are linked to antigen recognition, signaling, and chaperone function. *Cd300e* encodes an activating immunoreceptor associated with myeloid cell activation, while *Pou2f2* (Oct2) is a transcription factor that can influence DC maturation. *Hspa8* participates in protein folding, while *Ifi30* is involved in antigen processing and presentation, and their reduced expression in NIK-deficient resDC2 may suggest subtle impairments in vesicular trafficking and antigen-handling capacity, even in the absence of broader transcriptional remodeling.

Similarly, within the Mac cluster, only a few DEGs were significant, with 21 significant DEGs for the Macs population (Fig. 3 I) and 36 for the MoMacs (Fig. 3 J). The downregulated DEGs for the NIK-deficient Macs included *Syngr2*, *Hspa8*, *Ly6i*, and *Il27rg*, indicating reduced stress response and cytokine-associated programs, while upregulated DEGs in Macs, including *Rac2*, *Lacc1*, *Ppp2r3a*, and *Crabp2*, suggest enhanced cytoskeletal and metabolic remodeling (Fig. 3 I). For the MoMac cluster, the downregulated genes included *Ifi30*, *S100a6*, *Vim*, *Hspa8*, and *Tmem176a*/b, which suggest reduced antigen-processing and chaperone-related activity. Conversely, genes associated with adhesion, Fc receptor signaling, and Mac differentiation, such as *Adgre1*, *Fcer1g*, *Ms4a7*, *Fcgr4*, *Rac2*, *Cd300e*, and *Pparg*, were upregulated in MoMacs from NIK$^{\Delta CX3CR1}$ mice. KEGG pathway enrichment of the combined Mac and MoMac DEGs (Fig. 3 K) identified significant enrichment of cell adhesion molecules, phagosome, antigen processing and presentation, neutrophil extracellular trap formation, and Th1/Th2 differentiation pathways. Together, these transcriptional shifts indicate that NIK deficiency in CX3CR1-expressing cells remodels Mac activation, affecting antigen processing and chaperone functions while enhancing pathways linked to phagocytosis, Fc receptor signaling, and tissue-adaptive Mac states.

Similarly, monocyte subsets showed broader changes. In Ly6C^{hi} monocytes, genes including *Cx3cr1*, *Saa3*, and *Tgfb1* were downregulated in NIK$^{\Delta CX3CR1}$ mice (Fig. S3 D), while Cxcl10$^+$ monocytes showed reduced expression of *Hspa8*, *Tmem176a/b*, and *Atf3* (Fig. S3 E). Ly6C^{lo} monocytes also downregulated *Rac2*, *Fcgr4*, *Clec7a*, and *Vcam1*, suggesting impaired antigen uptake and adhesion capacity (Fig. S3 F). KEGG analysis of DEGs across all monocyte clusters revealed enrichment for phagosome, cell adhesion, efferocytosis, and antigen presentation pathways (Fig. S3 G), supporting a role of NIK in maintaining core monocyte immune functions.

These findings suggest that the downregulated genes in NIK$^{\Delta CX3CR1}$ myeloid cells may play crucial roles in the immune response, particularly in the processing and presentation of antigens to T cells.

Reduced antigen-presenting capabilities of myeloid cell populations before EAE onset

To confirm the results of the scRNA-seq data on the protein level, we isolated the dLN of NIK$^{\Delta CX3CR1}$ and control mice 5 days after MOG immunization and subjected them to high-dimensional flow cytometry (HDCyto) analysis. In the analysis, we excluded neutrophils and eosinophils and focused on the CD11b$^+$ cells, which include the monocytes, Macs, and DC2 populations of interest. UMAP and FlowSOM analysis identified eight clusters, which were annotated based on their marker expression (Fig. 4, A and B). In agreement with the scRNA-seq data, we observed an increase in Ly6C^{lo} monocytes in our NIK$^{\Delta CX3CR1}$ mice (Fig. 4 C). Importantly, we also found a decrease in the expression of costimulatory molecule CD80 in the Macs, moDC, and resDC2 clusters (Fig. 4 D). In the migDC2s, we did not detect any change in the expression level of CD80 between the control and NIK$^{\Delta CX3CR1}$ mice. However, we did observe a reduced expression of the costimulatory molecule CD86 on the migDC2s of NIK$^{\Delta CX3CR1}$ mice (Fig. 4 D). Upon examining the expression of PD-L1, a known promoter of immune tolerance (Sage et al., 2018; Waisman et al., 2017), we found a decreased expression of this marker on the cDC2 and migDC2 populations of NIK$^{\Delta CX3CR1}$ mice (Fig. 4 D). This finding further supports our hypothesis that the protection against EAE present in NIK$^{\Delta CX3CR1}$ mice is not due to the induction of tolerance but rather to impaired APC function.

In addition to CD80 and CD86, we also found that the gene expression of CD44 was reduced in the migDCs of NIK$^{\Delta CX3CR1}$

Downloaded from http://rupress.org/jem/article-pdf/223/4/e20242294/2027553/jem_20242294.pdf by guest on 31 May 2026

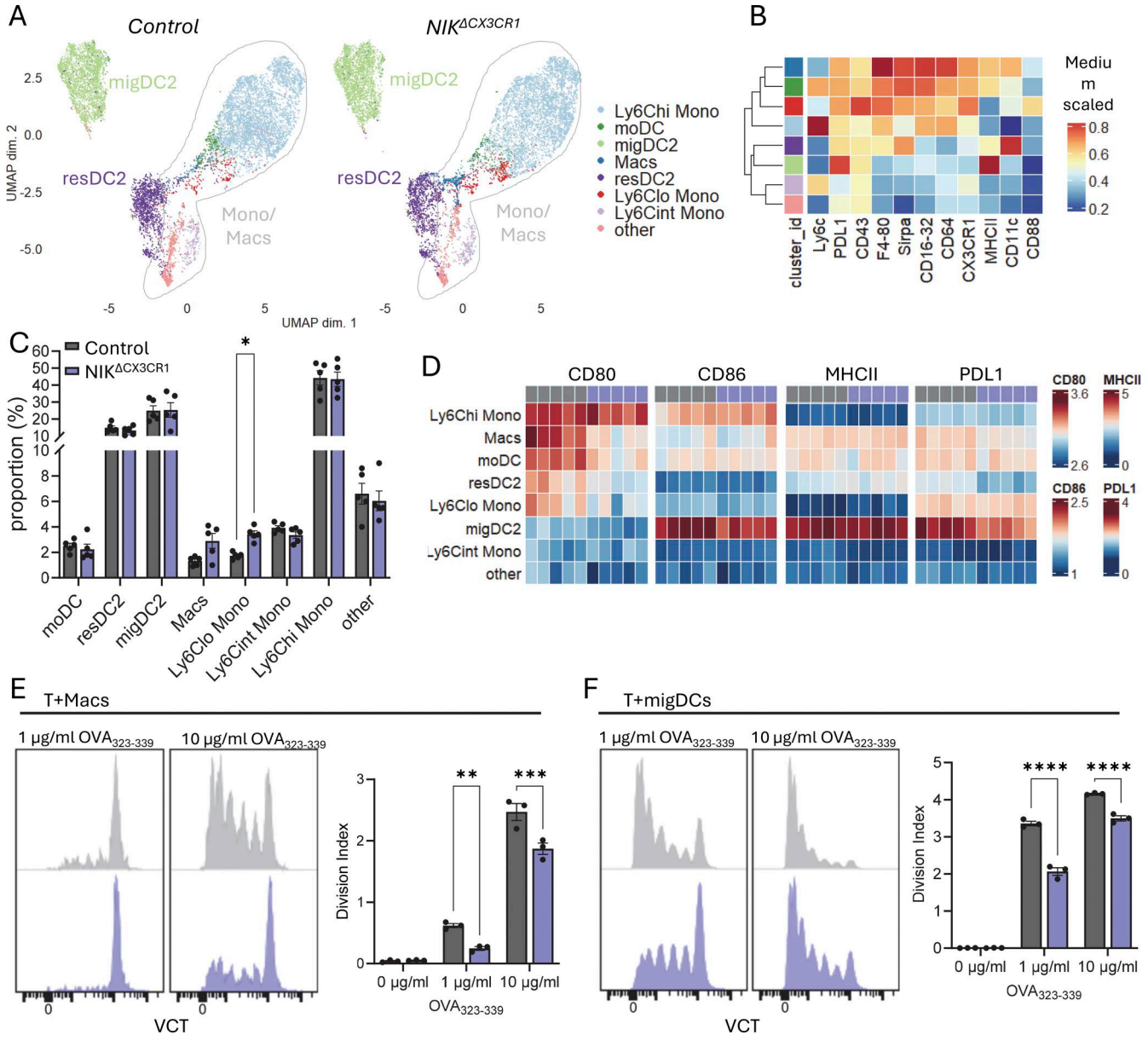

Figure 4. **Reduced costimulatory marker expression on myeloid cells and reduced antigen-presenting capabilities. (A and B)** UMAP map displaying 50,000 randomly sampled cells from the dLN of NIK$^{\Delta CX3CR1}$ (n = 5) and littermate controls (n = 5) analyzed by flow cytometry, focusing on CD11b$^+$ monocyte, Mac, and DC subsets 5 dpi. **(B)** Heatmap with median marker expression values for each population shown in the UMAP. **(C)** Relative frequencies of Ly6C^{high} monocytes (Mono), Ly6C^{int} Mono, Ly6C^{lo} Mono, ResDC2, MigDC2, MoDCs, Macs, other, pregated on CD11b$^+$ cells, and dead cells, duplicates, T and B cells, neutrophils, and eosinophils were excluded. **(D)** Median (arcsinh-transformed) expression of CD80, CD86, MHCII, and PD-L1 across the eight identified myeloid cell populations. **(E and F)** Representative flow cytometry histograms showing CTV dilution of OT-II CD4$^+$ T cells cocultured with either sorted Macs (T + Macs) (E) or migratory dendritic cells (T + migDCs) from dLNs (F) from control or NIK$^{\Delta CX3CR1}$ mice. Accompanying graphs show the Division Index, reflecting the average number of divisions per input cell. Cells were pulsed with the indicated concentrations of OVA$_{323-339}$ peptide for 1 h prior to coculture. Data are shown as the mean ± SEM and analyzed using two-way ANOVA with Šídák's multiple comparisons test. *P < 0.05, **P < 0.01, ***P < 0.001, ****P < 0.0001. dpi = days after immunization. Each dot represents one mouse. Data are from at least two independent experiments. CTV, CellTrace Violet.

mice (Fig. 3 G). CD44 is of special interest, as its expression is important for the entry of migDCs to the T cell zone in the LNs and subsequently for the activation of T cells (Weiss et al., 1997; Termeer et al., 2003). Although we did not see changes in the populations of migDCs (MHCII^{hi}CD11c^{int}), including migDC1 (CD11b$^-$), migDC2a (CD11b$^+$ESAM$^+$), and migDC2b (CD11b$^+$ESAM$^-$) 3 days after MOG immunization (Fig. S5 A), we identified a decrease in the expression of CD44 in the migDC2 populations but not migDC1s (Fig. S5 B), which confirms our scRNA-seq data. These findings indicate that NIK expression specifically in migDC2 may be critical for the activation of antigen-specific CD4$^+$ T cells.

To functionally assess whether APCs from NIK$^{\Delta CX3CR1}$ mice have impaired antigen presentation compared with their littermate controls, we performed an *in vitro* antigen presentation assay using sorted LN-derived APC subsets. ResDC2s

Downloaded from http://rupress.org/jem/article-pdf/223/4/e20242294/2027553/jem_20242294.pdf by guest on 31 May 2026

(CD11c^{high}MHCII^{int}CD11b^{+}), migDCs (CD11c^{int}MHCII^{high}), and Macs (F4/80^{+}CD11b^{+}) were isolated, pulsed with $OVA_{323-339}$ peptide for 1 h, and cocultured with CD4^{+} OT-II T cells. Using exogenous peptide isolates MHCII presentation and the formation of the immune synapse while bypassing antigen digestion and processing. This approach mirrors our *in vivo* EAE induction with the MOG_{35-55} peptide. T cell proliferation was measured after 4 days by dye dilution analysis. OT-II cells cocultured with NIK-deficient migDCs or Macs showed markedly reduced proliferation compared to those cultured with control APCs (Fig. 4, E and F), whereas resDC2s did not show significant differences between genotypes (Fig. S5 C). To further assess T cell activation, we quantified PD-1 expression on OT-II cells following coculture with the different APC subsets (Fig. S5 D). OT-II cells stimulated by migDCs or resDC2s from NIK$^{\Delta CX3CR1}$ mice showed higher frequencies of PD-1^{+} OT-II cells compared with those stimulated by control APCs, despite the overall reduced proliferative capacity observed in the migDC condition. In contrast, NIK-deficient Macs induced lower levels of PD-1 expression, consistent with their impaired ability to drive OT-II activation.

Taken together, our data demonstrate that NIK deficiency in myeloid cells modifies antigen-presenting ability in various APC subsets, with the most pronounced effects observed in migDCs and Macs. While resDC2s maintain the ability to induce T cell proliferation, the different subsets cause distinct PD-1 activation patterns. These findings suggest that NIK not only regulates the extent of T cell expansion but also modulates the qualitative aspects of the T cell response.

NIK regulates the expression of Il23a

Activation of the noncanonical NF-κB pathway results in the production of several cytokines and chemokines, which are essential for the immune and stress response (Sun, 2017). We performed an *in vitro* experiment to examine mRNA levels of different cytokines in CD11b^{+} myeloid cells after stimulating them with anti-CD40 or LPS (Fig. 5 A). We could not detect significant differences in the mRNA levels of the inflammatory cytokines *Il12a*, *Il6*, and *Il1b* after stimulation with anti-CD40 (Fig. 5, B–D), but observed a decrease of the pro-inflammatory cytokine *IL23a/p19* in the CD11b^{+} cells from NIK$^{\Delta CX3CR1}$ mice (Fig. 5 E). We could further see an increase in the anti-inflammatory cytokine *Il10* in cells of NIK$^{\Delta CX3CR1}$ mice after LPS induction but not significantly after anti-CD40 stimulation (Fig. 5 F).

IL-23 is a vital pro-encephalitogenic cytokine produced by APCs and essential for T cells to become encephalitogenic (Jie et al., 2018; Cua et al., 2003; Becher et al., 2002). To determine whether the T cells from NIK$^{\Delta CX3CR1}$ mice would acquire encephalitogenic properties after culturing them with IL-23 and investigate the notion that the reduced production of IL-23 could account for our EAE phenotype, we induced passive EAE in mice lacking the *Rag1* gene and therefore mature T and B cells (Rag^{KO}). We isolated cells from dLN and spleen of MOG-immunized NIK$^{\Delta CX3CR1}$ and control mice, and cultured them under conditions promoting encephalitogenic T_H cell development via the addition of IL-23, MOG, and anti-IFNγ before transferring them into Rag^{KO} recipients (Fig. 5 G). Prior to transfer of the T cells, we noted a reduced expression of GM-CSF and IL-17A in NIK$^{\Delta CX3CR1}$ donor cells compared with control donor cells (Fig. 5 H). Interestingly, T cells from NIK$^{\Delta CX3CR1}$ donor mice were still able to induce EAE in the Rag^{KO} recipients (Fig. 5 I). However, when comparing the disease score to the recipients who received cells from control mice, we could see a significantly reduced score, which could also be seen when comparing the area under the curve and maximum EAE score (Fig. 5, I, J, and L). Furthermore, we could observe a delay in the onset of EAE in the recipients who received T cells from NIK$^{\Delta CX3CR1}$ donors (Fig. 5 K). This suggests that adding IL-23 to the primed T cells of NIK$^{\Delta CX3CR1}$ mice could partially restore their encephalitogenic phenotype.

Overall, these results suggest that while the noncanonical NF-κB pathway influences the production of multiple cytokines, the specific reduction of IL-23 expression by NIK$^{\Delta CX3CR1}$ myeloid cells plays a pivotal role in limiting the encephalitogenic potential of T cells and contributes to the observed EAE resistance.

Discussion

Understanding the mechanisms by which myeloid cells, such as APCs, regulate immune responses is crucial for unraveling the complexities of autoimmune disease pathology. In this study, we show that the myeloid cell compartment of mice lacking NIK in myeloid cells displays a dysregulation in genes associated with antigen presentation and migration, along with reduced IL-23 production and antigen-presenting capabilities. This resulted in decreased priming of T cells, specifically the production of the inflammatory cytokines IL-17A and, to some extent, GM-CSF. Notably, transferring *ex vivo* MOG/IL-23–activated T cells from immunized NIK$^{\Delta CX3CR1}$ mice into Rag^{KO} mice was able to reconstitute disease susceptibility in donor mice, as seen by the development of clinical EAE scores, suggesting the lack of IL-23 production by the CX3CR1-expressing myeloid cells as the confounding factor in disease resistance.

The CX3CR1-Cre targets multiple cell populations, which include subpopulations of cDC2s, monocytes, Macs, and microglia (Yona et al., 2013). A recent study describing NIK-deficient microglia reported reduced disease symptoms and fewer infiltrating cells in the late phase of EAE (Jie et al., 2021). Although our study did not reveal significant differences in EAE progression in the NIK$^{\Delta MG}$ mice, which lack NIK in only microglia, it is important to note that our study focused on the peak of EAE, during which we did not observe differences in microglial activation or infiltrating cells between NIK$^{\Delta MG}$ and controls. This finding aligns with the results of Jie et al. (2021), who also reported no differences during the peak of EAE but observed differences only at later stages of the disease. This suggests that NIK in microglia may play a role in the second wave of infiltrating cells into the CNS (Jie et al., 2021). Based on our data and the findings published by Jie et al., we can confidently conclude that microglia are unlikely to be involved in the resistance to EAE observed in the NIK$^{\Delta CX3CR1}$ mice. Our findings rather suggest that the lack of NIK in peripheral CX3CR1-expressing myeloid cells is responsible for this resistance.

Peripheral myeloid cells expressing CX3CR1 include moDCs and a subset of cDC2s, which are critical contributors to immune responses by bridging innate and adaptive immunity. However,

Downloaded from http://rupress.org/jem/article-pdf/223/4/e20242294/2027553/jem_20242294.pdf by guest on 31 May 2026

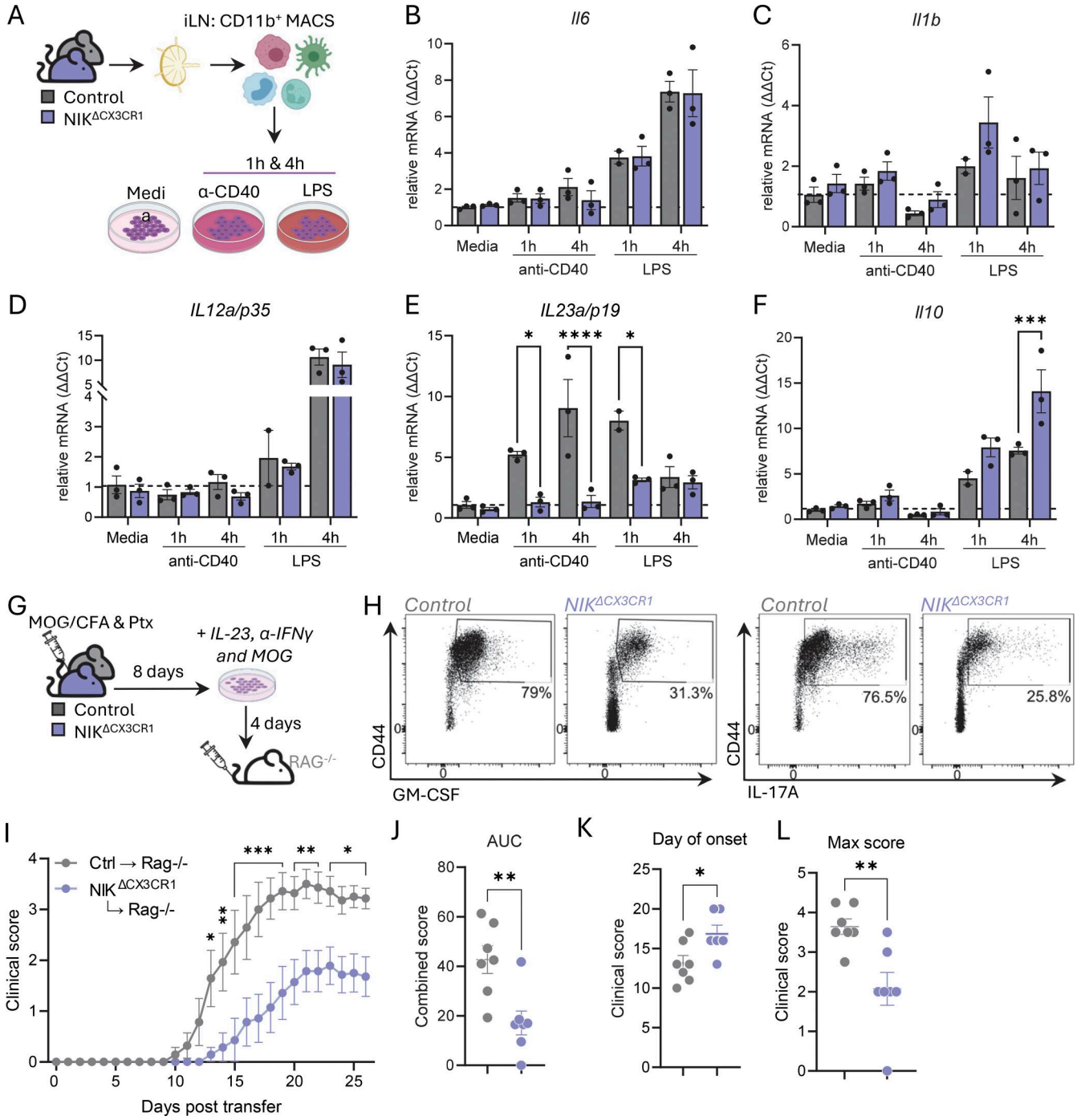

Figure 5. **NIK deletion in myeloid cells results in reduced Il23a, which is partially responsible for the resistance against EAE. (A–F)** CD11b$^+$ cells were isolated from the dLNs of NIK$^{\Delta CX3CR1}$ and littermate controls and were cultured with or without anti-(α)CD40 or LPS for 1 or 4 h. Relative mRNA levels (ΔΔCt) of (B) Il6, (C) Il1b, (D) Il12a/p35, (E) Il23a/p19, and (F) Il10, and mRNA levels of each sample were normalized against the housekeeping gene HPRT and the medium control of the corresponding cytokine. Dotted line = medium control. **(G)** NIK$^{\Delta CX3CR1}$ and littermate controls were immunized with MOG_{35-55}/CFA and PTx; isolated cells from dLNs and spleen were cultured for 4 days with MOG_{35-55}, IL-23, and anti-IFNγ before being injected into Rag−/− recipient mice. **(H)** Flow cytometry gating for CD44/GM-CSF and CD44/IL-17A of the donor cells before being injected into recipient mice, pregated on single/live/CD90$^+$/CD4$^+$ cells. **(I)** Passive transfer EAE disease course of recipients receiving control cells (Ctrl → Rag$^{-/-}$) or NIK$^{\Delta CX3CR1}$ cells (NIK$^{\Delta CX3CR1}$ → Rag$^{-/-}$). **(J)** AUC. **(K)** Day of onset. **(L)** Maximum disease score. Data in graphs are shown as the mean ± SEM and analyzed using two-way ANOVA with Šídák's multiple comparisons test or two-tailed unpaired Student's *t* test. *P < 0.05, **P < 0.01, ***P < 0.001, ****P < 0.0001. Each dot represents one mouse. Data are from at least two independent experiments. dpi = days after immunization. AUC, area under the curve.

Downloaded from http://rupress.org/jem/article-pdf/223/4/e20242294/2027553/jem_20242294.pdf by guest on 31 May 2026

the exact role of these cells in EAE is still debated. Studies depleting CD11c-expressing cells have shown mixed results on the role of DCs during EAE (Yogev et al., 2012; Luu et al., 2021; Isaksson et al., 2012). Katakam et al., who utilized a cell-specific deletion of NIK in CD11c-positive cells, demonstrated that it is dispensable for $CD4^+$ T cell priming and EAE development (Katakam et al., 2015). However, in our hands, the deletion of NIK with CD11c-Cre resulted in a similar resistance against EAE as seen in the $NIK^{\Delta CX3CR1}$ mice. These results are further supported by other published data showing a role of NIK in DCs during EAE (Hofmann et al., 2011; Huang et al., 2018). The discrepancy may be due to differences in experimental protocols, particularly the concentration of MOG_{35-55}, which was lower in our study. The high concentration of MOG used in the Katakam et al. study might obscure a difference in EAE scores.

Considering the similar EAE phenotype in both CD11c-Cre and CX3CR1-Cre mice, we conclude that the effect might stem from $CX3CR1^+CD11c^+$ double-positive populations. This would include multiple APC subsets, such as cDC2, moDC, MoMac, migDC, and certain Mac subsets. Indeed, our reporter analysis at the onset of disease (5 dpi) confirmed that all subsets were RFP-positive in $NIK^{\Delta CX3CR1}$, indicating successful NIK targeting within these populations. While we focused on this early time point to capture the priming phase, it remains possible that RFP expression, and thus the relative contributions of different $CX3CR1^+$ subsets, shifts during the earlier or later stages of the disease.

Both moDCs and cDC2s have been shown to be important in T cell priming, with moDCs promoting T_H polarization and cDCs promoting T_H priming (Chow et al., 2016). A recent study has demonstrated two cDC2 populations in the spleen and LNs of mice: T-bet^+ cDC2a and T-bet^- cDC2b. This cDC2b subset expresses CX3CR1 and is shown to be more pro-inflammatory by producing higher levels of IL-6 and TNFα and is more potent in inducing T_H1 and T_H17 differentiation than cDC2a (Brown et al., 2019). This further suggests that the $CX3CR1^+CD11c^+$ cDC2a subset might play a substantial role in our observed EAE phenotype.

We were indeed able to see in our scRNA-seq data from dLNs that resDC2s, together with Macs, displayed the highest antigen-presenting score, and that these populations were notably reduced in the $NIK^{\Delta CX3CR1}$ mice. However, the migDC population showed the greatest transcriptional changes, with the highest number of DEGs. KEGG pathway analysis of DEGs within the migDC cluster revealed enrichment for antigen processing and presentation, as well as broader immunoactivation pathways, suggesting that NIK is required to maintain the transcriptional program that equips migDCs for efficient T cell priming. We also observed decreased protein expression of the costimulatory molecules CD80 and CD86 in certain APC subsets, including migDCs and cDC2s. A decrease in these costimulatory molecules on the APCs could help explain the decrease in T cell priming we observed prior to EAE onset. Functionally, the most pronounced deficits in antigen presentation capacity were observed in migDCs from $NIK^{\Delta CX3CR1}$ mice, not the resDC2 population. However, both populations induced higher PD-1 expression on the OT-II T cells. Together, these findings suggest that APCs from $NIK^{\Delta CX3CR1}$ mice deliver an imbalanced combination of activation signals with reduced costimulation and reduced PD-L1. This likely results in a dysregulated T cell response, with migDCs showing the most pronounced effect.

Macs were similarly affected by the loss of NIK, showing shifts in gene expression and activation state. In the antigen presentation assay, Macs isolated from $NIK^{\Delta CX3CR1}$ mice displayed a diminished capacity to present antigen, similar to the migDCs, suggesting an impaired ability to support T cell activation. However, the Mac population induced lower PD-1 expression on OT-II cells, which is consistent with a weaker or insufficient activation signal. This further indicates that $NIK^{\Delta CX3CR1}$ Macs are less able to deliver the cues required for productive T cell priming. For this assay, the Macs were sorted as $CD11b^+F4/80^+$ cells, a subset that most likely includes the $Ly6C^{lo}$ monocyte subset, which also expresses F4/80. These $Ly6C^{lo}$ monocytes are thought to be more anti-inflammatory and were found to be increased in the LNs of $NIK^{\Delta CX3CR1}$ mice early after EAE induction. Studies have shown that $Ly6C^{hi}$ monocytes are able to infiltrate into the tissue and subsequently differentiate into $Ly6C^{lo}$ monocytes and Macs (Yona et al., 2013; Miyake et al., 2024; Auffray et al., 2007). The population identified as $Ly6C^{lo}$ monocytes in our scRNA-seq data likely consists of $Ly6C^{lo}$ Macs or cells transitioning into Macs, as they also express the Mac marker *Adgre1* (F4/80). These $Ly6C^{lo}$ Macs have been associated with anti-inflammatory or tissue-protective roles in several models (Egawa et al., 2013; Brunet et al., 2016; Kalinski et al., 2020; Li et al., 2022b). Transcriptomic profiling of the Mac and monocyte clusters further revealed a shift toward an anti-inflammatory phenotype in the $NIK^{\Delta CX3CR1}$ mice. Specifically, the MoMac and $Ly6C^{lo}$ cluster showed increased expression of genes associated with anti-inflammatory Macs, including *Pparg2* and *Atf3* (Sha et al., 2017; Croasdell et al., 2015). In addition, *in vitro* stimulation of myeloid cells led to an increase in *Il10* mRNA in the $NIK^{\Delta CX3CR1}$ mice.

Our findings suggest that NIK has a role in both antigen-presenting capacity and the inflammatory state of the myeloid compartment and may regulate different myeloid populations through distinct mechanisms, thereby limiting efficient T cell activation during the initial stages of EAE.

More interestingly, we demonstrated that NIK is essential for *Il23a* production, which is essential for EAE induction. The involvement of NIK in regulating IL-23 production is confirmed by previously published data (Jie et al., 2018; Huang et al., 2018). Jie et al. demonstrated that in a colitis model, NIK-activated non-canonical NF-κB induces the expression of IL-23 in DCs, contributing to the maintenance of T_H17 cells in the gut (Jie et al., 2018). IL-23 has further been shown to be essential for T cell differentiation into T_H17 cells, the production of GM-CSF by encephalitogenic T cells, and the development of EAE (Jie et al., 2018; Cua et al., 2003; El-Behi et al., 2011). However, our data indicate that in the context of CNS autoimmunity, NIK acts as a comprehensive regulator of myeloid cell function. Specifically, we observed that exogenous IL-23 only partially restored EAE susceptibility, suggesting that the role of NIK extends beyond a single cytokine axis. Our scRNA-seq and functional antigen presentation assays further demonstrate that NIK deficiency impairs the broader cellular programming of myeloid cells. Unlike previous models, our results show that NIK drives the full

Downloaded from http://rupress.org/jem/article-pdf/223/4/e20242294/2027553/jem_20242294.pdf by guest on 31 May 2026

functional profile required for myeloid cells to prime T cells, including antigen presentation and IL-23 production.

Studies have also revealed that IL-23 is elevated in MS patients and correlates with T_H17 cells and disease, which makes it an interesting target for the treatment of MS. Furthermore, the inhibition of IL-23 by using antisense oligonucleotides has been shown to downregulate IL-23 and TNF-α production and upregulate IL-10 production in moDC cultures from MS patients (Vaknin-dembinsky et al., 2006). It will be fascinating to investigate further which CX3CR1-expressing cells produce IL-23 during EAE and how this production affects disease development. This could open up new avenues for understanding and potentially treating EAE and MS.

Given its role as a key regulator in the noncanonical NF-κB pathway, which is involved in immune regulation and inflammation, targeting NIK represents a novel therapeutic strategy for MS and other autoimmune diseases. Under normal conditions, NIK levels are kept low in most cell types, which helps maintain cellular homeostasis. The fact that mice and humans with loss-of-function mutations in NIK survive suggests that NIK is not essential for life, making it a viable target for therapeutic intervention in autoimmune diseases without causing severe systemic effects. We were able to show that NIK targets multiple aspects of the immune system. Targeting NIK would not only regulate the pro-inflammatory cytokine IL-23 but could also affect the priming of T cells and regulate the activation of myeloid cells. Recent research has highlighted the potential of NIK inhibition in various therapeutic contexts (Cheng et al., 2021). For example, NIK inhibition has shown promise as a target for cancer therapy due to its role in cell survival and proliferation (Li et al., 2022a). Moreover, NIK inhibitors have been suggested for the treatment of sepsis, given their ability to modulate inflammatory responses (Zhang et al., 2024). Notably, a genome-wide association study identified NIK as a susceptibility gene for MS, directly linking it to the pathogenesis of this autoimmune disease (Beecham et al., 2013). This suggests that NIK inhibitors could be a potential therapeutic intervention during MS pathology, offering a ray of hope in the treatment of autoimmune diseases.

Materials and methods

Mice

All mice used were on the C57BL/6J background and housed under specific-pathogen-free conditions. $NIK^{fl/fl}$ mice were generated by TaconicArtemis and crossed to CX3CR1-Cre mice ($NIK^{\Delta CX3CR1}$), CX3CR1-Cre^{ERT2} mice ($NIK^{\Delta MG}$) (Yona et al., 2013), and CD11c-Cre mice (Caton et al., 2007) ($NIK^{\Delta DC}$). $NIK^{fl/fl}$ Cre-negative and $NIK^{fl/wt}$ Cre-positive littermates were used as controls. Rosa26-tdRFP reporter mice were crossed with CX3CR1-Cre and CD11c-Cre for lineage-tracing experiments (Luche et al., 2007). For AT-EAE experiments, Ly5.1 mice (B6.SJL-Ptprca-Pepcb/BoyCrl) were used as donor mice. For 2D2 T cell transfer experiments, 2D2 mice (Bettelli et al., 2003) were used.

Tamoxifen treatment

A 20 mg/ml solution of tamoxifen (Sigma-Aldrich) was prepared by suspension in olive oil (Sigma-Aldrich) at 37°C for 2 h on a shaker. Pups of the $NIK^{\Delta MG}$ strain were injected subcutaneously with 2 mg of tamoxifen, 2 days apart at P14 and P16. $NIK^{fl/fl}$ littermate controls were treated equally.

Active EAE induction

An emulsion of 50 µg MOG_{35-55} peptide (GenScript) and CFA (BD Biosciences) supplemented with heat-inactivated *Mycobacterium tuberculosis* H37RA (BD Biosciences) was injected subcutaneously into the tail base. 150 ng of pertussis toxin (PTx, List Biological Laboratories) in PBS was injected i.p. on the same day as the MOG immunization and again 2 days later. The mice were weighed daily and scored for clinical signs of EAE. The clinical assessment scale ranges from 0 to 5 as follows: 0: no disease; 0.5: limb tail; 1: paralyzed tail; 1.5: weakened righting reflex; 2: no righting reflex; 3: partial paralysis of hind legs; 3.5: paralysis of both hind legs; 4: upper body starts to lower, 4.5: mouse lies on one body side without moving, 5: mouse is found dead.

Adoptive transfer EAE

Donor mice were immunized for EAE, as described above. At 8 days after immunization (dpi), single-cell suspensions of spleen and dLNs (inguinal and para-aortic) were prepared and cultured in T cell media (RPMI 1640 with 50 µM β-mercaptoethanol, 25 mM HEPES, 2% FCS, 1% penicillin–streptomycin, 1 mM sodium pyruvate, and 1 mM NEAA) containing 15 ng/ml IL-23 (Sino Biological), 10 µg/ml anti-IFNG (BioXCell), and 20 µg/ml MOG_{35-55} peptide. After 4 days, cells were harvested and examined for blasting lymphocytes, as based on forward and side scatter properties in flow cytometry. Cell suspensions were adjusted to 50×10^6 blasting cells/ml, and 100 µl of this suspension was injected i.v. into the tail veins of recipient mice, accompanied by i.p. injections of PTx (150 ng) the same day and 2 days later. Mice were weighed daily, and the clinical scores were assessed according to the scoring system described above.

2D2 T cell transfer

Single-cell suspensions of the spleen and dLN (inguinal) of 2D2 mice (Bettelli et al., 2003) were prepared, and $CD4^+$ cells were purified using $CD4^+$ T Cell Isolation Kit according to the manufacturer's protocol (130-104-454; Miltenyi Biotec) using the LS columns (Miltenyi Biotec). 10^4 2D2 cells were injected i.v. in the tail vein of experimental mice 1 day before EAE induction. Cells from the spleen and dLNs were isolated 6 days after MOG immunization.

Leukocyte isolation from the CNS

Mice were deeply anesthetized by inhalation with isoflurane, then transcardially perfused with 15–20 ml sterile NaCl prior to organ isolation. Brain and spinal cord were digested in collagenase type II (2 mg/ml, Gibco) and DNase type I (0,05 mg/ml, Roche) in HBSS with calcium and magnesium (Sigma-Aldrich) for 30 min at 37°C. CNS homogenates were passed through a 70-mm cell strainer and put into a discontinuous 30%:37%:70% Percoll (Sigma-Aldrich) gradient and centrifuged for 40 min without brakes at 500 *g* and 16°C. Myelin was discarded, and the 70/37% interphase was carefully collected for flow cytometry analysis.

Downloaded from http://rupress.org/jem/article-pdf/223/4/e20242294/2027553/jem_20242294.pdf by guest on 31 May 2026

For RNA analysis of microglia, a simplified 30% Percoll gradient was used to remove myelin. The cell pellet was then subjected to positive selection of CD11b$^+$ cells with magnetic microbeads (130-049-601; Miltenyi Biotec) according to the manufacturer's instructions. The purified microglial fraction was used for subsequent RNA extraction.

Leukocyte isolation from secondary lymphoid organs for flow cytometry

Spleen and LNs were mechanically dissociated in PBS/2% FCS and filtered through a 40-mm cell strainer. Erythrocytes were removed from the spleen by ammonium–chloride–potassium lysis. For myeloid cell isolation, the spleen and LNs were digested in collagenase type II (1 mg/ml) and DNase type I (0,1 mg/ml) in PBS with calcium and magnesium while shaking at 37°C for 30 min. EDTA was added to a 10 mM final concentration, and the cell suspension was passed through a 70-mm cell strainer.

For cytokine staining, cells were reactivated prior to staining in T cell media containing 50 ng/ml PMA (P1585; Sigma-Aldrich), 500 ng/ml ionomycin (PK-Ca577-1565; PromoKine), and 1 µg/ml brefeldin A (B6542; Sigma-Aldrich) for 4 h at 37°C. Or isolated cells were reactivated with 20 µg/ml MOG_{35-55} peptide in T cell media together with 1 µg/ml brefeldin A at 37°C for 6 h.

Flow cytometry

Monoclonal, murine-specific antibodies from BioLegend included anti-CD4 (GK1.5), anti-CD8a (53-6.7), anti-CD11b (M1/70), anti-CD45 (30-F11), anti-CD88 (20/70), anti-CD90.1 (OX-7), anti-CD90.2 (53-2.1), anti-Ly6C (HK1.4), anti-Sirpα (P84), anti-CD154 (MR1), anti-CX3CR1 (SA011F11), anti-ESAM (1G8/ESAM), and anti-GM-CSF (MP1-22E9). Antibodies from BD Biosciences included anti-CD16/32 (2.4G2), anti-CD19 (1D3), anti-CD43 (F7), anti-CD45 (30-F11), anti-CD80 (16-10A1), anti-CD86 (GL1), anti-CD274 (MIH5), anti-CX3CR1 (Z8-50), anti-Ly6G (1A8), anti-A/I-E (M5/114.15.2), anti-TCR vβ11 (RR3-15), anti-CD11c (N418), and F4.80 (T45-2342). Antibodies from eBioscience included anti-CD44 (IM7), anti-CD11b (M1/70), anti-Foxp3 (FJK-16s), anti-IFNγ (XMG1.2), and anti-IL-17A (eBio17B7).

Before antibody staining, the single-cell suspensions of the different organs were resuspended in FACS buffer (PBS with 2% FCS and 2 mM EDTA) with Fc-block (5 µg/ml, BioXCell) for 20 min at 4°C. Next, cells were incubated with surface antibodies in FACS buffer for 30 min at 4°C. Afterward, where indicated, cells were fixed and permeabilized with Cytofix/Cytoperm (BD Bioscience) for cytokine stainings or Foxp3/Transcription Factor Staining Buffer Set (eBioscience) and stained overnight at 4°C with intracellular antibodies.

Cells were acquired with FACSCanto II or FACS symphony cytometers (BD Bioscience) using FACSDiva software (BD Bioscience). Flow cytometry data were analyzed with FlowJo software version 10 (BD Bioscience). For all analyses, doublets (forward and side scatter properties) and dead cells (dye inclusion, fixable viability dye APC-eF780; eBioscience) were excluded.

For HDCyto analysis, cells were pregated in FlowJo, excluding doublets, dead cells, neutrophils, eosinophils, and NK, B, and T cells. The CD11b$^+$ populations were exported for each sample and further analyzed in RStudio as described in https://f1000research.com/articles/6-748 (Nowicka et al., 2019). In short, the packages CATALYST and FlowSOM were used to cluster cells and the nonlinear dimensionality reduction technique, UMAP, was used to visualize the clusters (1,000 cells randomly selected per sample).

In vitro antigen presentation assay

Purified APCs from LNs were flow cytometrically sorted as either resident cDC2s (MHCII^{int}CD11c^{high}CD11b$^+$), migratory DCs (CD11c^{int} MHCII^{high}), or Macs (F4/80$^+$CD11b$^+$). A total of 1 × 10^4 cells from each population were plated in 96-well round-bottom plates and pulsed with $OVA_{323-339}$ peptide (1 µg/ml and 10 µg/ml) for 60 min at 37°C, 5% CO_2. Cells were then extensively washed with warm medium to remove unbound peptide and cultured with 1 × 10^5 CellTrace Violet–labeled (Thermo Fisher Scientific) OT-II CD4$^+$ T cells at an APC:T cell ratio of 1:10. After 4 days, cells were harvested, and stained with viability dye and anti-CD4 antibodies, and proliferation of viable OT-II CD4$^+$ T cells was assessed by CellTrace Violet dilution using flow cytometry. Control conditions included T cells alone and unpulsed APCs.

In vitro stimulation of myeloid cells

Cells from the spleen and LNs were isolated with enzymatic digestion, as described above. Myeloid cells were purified using CD11b$^+$ Cell Isolation Kit according to the manufacturer's protocol (130-049-601; Miltenyi Biotec) using the LS columns (Miltenyi Biotec). 5 × 10^4 cells were plated in media (RPMI-1640 with 50 µM β-mercaptoethanol, 25 mM HEPES, 2% FCS, 1% penicillin–streptomycin, 1 mM sodium pyruvate, and 1 mM NEAA) with 10 µg/ml anti-CD40 (BioXCell) or 1 µg/ml LPS (Sigma-Aldrich).

RNA extraction and qPCR

RNA was extracted from isolated cells using ReliaPrep RNA Cell Miniprep System (Promega) according to the manufacturer's instructions. cDNA was synthesized using 200–1000 ng of total RNA with the Superscript II reverse transcriptase (Invitrogen) and subsequently used for qPCR, which was performed with the StepOnePlus Real-Time PCR System (Life Technologies) using SYBR Green (Promega). Fold enrichment was calculated using the Delta–Delta CT method normalized to hypoxanthine–guanine–phosphoribosyltransferase (*Hprt*) as a housekeeping reference. Primers for *Map3k14* were custom-ordered with the following sequences: forward 5′-CCTCGGGAAGCGCCAAG-3′ and reverse 5′-GAAGGAGCCTCTGCCCACCC-3′ (Metabion). Primers for *Hprt*, *Il23a*, *Il12a*, *Il6*, *Il1b*, and *Il10* were obtained as QuantiTect Primer Assays (Table 1).

16S rRNA sequencing and analysis

Fecal samples were collected from age-matched mice and stored at −80°C until processing. DNA extraction, 16S rRNA library preparation, sequencing, and bioinformatics analysis were performed by Novogene. The V3–V4 region of the bacterial 16S rRNA gene was amplified using barcoded primers and sequenced on an Illumina NovaSeq platform according to Novogene standard protocols.

Raw paired-end reads were demultiplexed, quality-filtered using fastp, and merged using FLASH. Chimera removal was

Downloaded from http://rupress.org/jem/article-pdf/223/4/e20242294/2027553/jem_20242294.pdf by guest on 31 May 2026

Table 1. **Primers used for qPCR**

Gene name/Commercial primers	Company
Mm_Hprt_1_SG QuantiTect Primer Assay	Qiagen (QT00166768)
Mm_Il23a_ 2_SG QuantiTect Primer Assay	Qiagen (QT01663613)
Mm_Il12a_1_SG QuantiTect Primer Assay	Qiagen (QT01048334)
Mm_Il6_1_SG QuantiTect Primer Assay	Qiagen (QT00098875)
Mm_Il1b_2_SG QuantiTect Primer Assay	Qiagen (QT01048355)
Mm_Il10_1_SG QuantiTect Primer Assay	Qiagen (QT00106169)

performed using VSEARCH against the SILVA reference database, and denoising was carried out with DADA2 within QIIME2 to generate amplicon sequence variants. Each sample yielded ∼30,000 reads, providing sufficient depth for downstream diversity and compositional analyses.

α-Diversity was calculated using the Shannon index, and β-diversity was assessed using weighted UniFrac distance metrics and visualized via PCoA. Relative abundance plots display the top 10 genera across samples. No significant differences in microbial diversity or composition were detected between genotypes.

Data files have been uploaded to the Gene Expression Omnibus public database (GSE318004).

Sample preparation for scRNA-seq

Cells from dLN were isolated from mice 4 dpi as described earlier. To enrich for myeloid cells, T and B cells were removed by using the CD19 microbeads and CD90.2 microbeads (MACS) (130-121-301, 130-121-278; Miltenyi Biotec) according to the manufacturer's protocol. Briefly, isolated cells were incubated with anti-CD90.2 and anti-CD19 MACS beads, washed, and then applied to prepared LD columns. The flow-through and 3× wash steps with MACS buffer were collected as this contained the enriched myeloid cells, while CD90 and CD19 cells were magnetically bound to the column and discarded afterward.

Isolated myeloid cells were trapped on a BD Rhapsody cartridge. Each sample was tagged with a unique sample tag in order to allow multiplexing of samples on the same cartridge (4 samples per cartridge). Samples were further processed according to BD Rhapsody workflow. Briefly, after passing a BD Rhapsody cartridge, cell capture beads were passed over the cartridge, cells were lysed, and the beads were retrieved. Whole-transcriptome libraries and sample tag libraries were created using BD WTA Amplification Kit (BD Rhapsody) with random primers followed by amplification and insertion of sequencing adaptors following the BD Rhapsody System WTA and Sample Tag Library Preparation Protocol (BD Biosciences). Quality control was performed with Invitrogen's Qubit HS assay, and fragment size was determined using Agilent's 2100 Bioanalyzer HS DNA Assay. Samples were then sent to Novogene Europe (Cambridge, UK) for sequencing (150 cycles; PE) aiming for ∼50.000 reads per cell.

The resulting raw data were preprocessed according to the Illumina standard protocol, and read alignment, counting, and demultiplexing were done in the BD Rhapsody pipeline, yielding 22,238 called putative cells overall with a mean of 65,437.95 aligned reads per cell.

scRNA-seq data analysis

Pipeline output was imported into RStudio software and further analyzed with the Seurat package (Hao et al., 2023). Steps were followed as described in vignettes/pbmc3k_tutorial.Rmd. Cells that contained <200 detected genes and a percentage of mitochondrial counts >12% were removed from subsequent analysis. Single-cell counts were normalized by scaling each cell's expression values by its total expression, multiplying by a factor of 10,000, and then applying a log transformation. Dimensionality reduction was performed using principal component analysis to identify the principal components that capture the most significant variance in the gene expression data. The first 15 principal components were selected for downstream analysis. A graph-based approach was employed for clustering. First, a shared nearest neighbor graph was constructed using the identified principal components. Then, the Louvain algorithm was applied to this graph to identify clusters of cells with similar expression profiles. A resolution parameter of 0.5 was used to determine the granularity of the clustering. Clusters were visualized using the UMAP technique and annotated according to ImmGen's (https://www.immgen.org/) data browser.

The cell signature for antigen presentation was added to the UMAP visualization using the UCell package. The following genes were included in the signature: *Cd81, Cd80, Cd40, Cd86, Ctss, Tnfsf9, Cd68, Mapk14, Icam1, Ciita, Clec4a2, Cd74, H2-Ab1, H2-Aa,* and *Cd274*.

Differential abundance testing was conducted using the Milo package (Dann et al., 2022). This method identifies changes in cell population frequencies between conditions, allowing us to detect shifts in cellular composition and abundance in a spatially aware manner.

To identify DEGs between groups, the FindMarkers function was used. DEGs were identified and sorted based on the following criteria: adjusted P <0.05, and Log2FC >0.1 and <−0.1. For KEGG pathway enrichment analysis, the enrichKEGG function from the clusterProfiler package (Wu et al., 2021) was employed. Pathways within the category Human Diseases were excluded from the dot plots.

Data files have been uploaded to the Gene Expression Omnibus public database (GSE285714).

Statistical analysis

All data are represented as the mean ± SEM. Statistical significance between groups was calculated with one-way or two-way ANOVA with Šídák's multiple comparisons analysis, Mann–Whitney U test, or Student's *t* test where applicable, using GraphPad Prism software (GraphPad Software). The P values are shown as follows: *P = 0.01–0.05; **P = 0.001–0.01; ***P < 0.001; ****P < 0.0001.

Online supplemental material

Fig. S1 shows neutrophils and monocytes at the peak of EAE. Fig. S2 characterizes EAE in NIK$^{\Delta MG}$ mice. Fig. S3 provides analysis of T_{reg} cell proportions in the dLNs, spleen, and CNS during

Downloaded from http://rupress.org/jem/article-pdf/223/4/e20242294/2027553/jem_20242294.pdf by guest on 31 May 2026

different EAE time points. Fig. S4 includes additional analysis of scRNA-seq, and Fig. S5 presents additional flow cytometry analysis of CD44 on DC subsets and antigen presentation assay data for resDC2s. Table S1 shows the DEGs for each cluster and KEGG results of the scRNA-seq data.

Study approval

All animal experiments were approved by the local administrations (Landesuntersuchungsamt Koblenz, Germany; Ministerium für Energiewende, Landwirtschaft, Umwelt und ländliche Räume, Kiel, Germany; approval number G 13-1-098). Experiments were performed in accordance with the guidelines from the Translational Animal Research Center, Mainz, Germany. All efforts were made to minimize suffering of the mice.

Data availability

The sequencing data generated in this study have been deposited in the Gene Expression Omnibus database. The 16S rRNA gene sequencing data are available under accession number GSE318004, and the scRNA-seq data are available under accession number GSE285714.

Acknowledgments

The authors would like to thank Lisa Johann, Arthi Shanmugavadivu, Elisa Blickberndt, and Aysan Poursadegh Zonouzi for their technical help. We are thankful to the Core Facility Flow Cytometry of the Research Center for Immunotherapy (FZI) for their support. We are grateful to all members of the A.W. laboratory for their assistance and suggestions.

This work was funded by grants from the Deutsche Forschungsgemeinschaft (German Research Foundation) project number 318346496–SFB1292/2 to T. Bopp and A. Waisman, project number 490846870—TRR355/1 to A. Waisman and T. Bopp, the Swiss National Science Foundation Project numbers 310030-219287 and 310030-188450 to B. Becher, and European Research Council under the European Union's Horizon 2020 research and innovation program grant agreement number 882424 to B. Becher.

Author contributions: Nishada S. Ramphal: conceptualization, data curation, formal analysis, investigation, methodology, project administration, validation, visualization, and writing—original draft, review, and editing. Xinyuan Liu: investigation. Ilaria Palagi: investigation. Rebecca Jasser: investigation. Alma N. Mohebiany: methodology, resources, and writing—review and editing. Matthias Klein: formal analysis and visualization. Frederike Westermann: formal analysis, investigation, and validation. Sinduya Krishnarajah: formal analysis and investigation. Tommy Regen: investigation, resources, supervision, validation, and writing—review and editing. Tobias Bopp: data curation, methodology, resources, and writing—review and editing. Burkhard Becher: conceptualization, funding acquisition, project administration, resources, supervision, and writing—original draft, review, and editing. Ari Waisman: conceptualization, funding acquisition, investigation, methodology, project administration, resources, supervision, and writing—original draft, review, and editing.

Disclosures: The authors declare no competing interests exist.

Submitted: 3 December 2024
Revised: 3 December 2025
Accepted: 5 February 2026

References

Amorim, A., D. De Feo, E. Friebel, F. Ingelfinger, C.D. Anderfuhren, S. Krishnarajah, M. Andreadou, C.A. Welsh, Z. Liu, F. Ginhoux, et al. 2022. IFNγ and GM-CSF control complementary differentiation programs in the monocyte-to-phagocyte transition during neuroinflammation. *Nat. Immunol.* 23:217–228. https://doi.org/10.1038/s41590-021-01117-7

Andreas, N., M. Potthast, A.-L. Geiselhöringer, G. Garg, R. de Jong, J. Riewaldt, D. Russkamp, M. Riemann, J.-P. Girard, S. Blank, et al. 2019. RelB deficiency in dendritic cells protects from autoimmune inflammation due to spontaneous accumulation of tissue T regulatory cells. *J. Immunol.* 203:2602–2613. https://doi.org/10.4049/jimmunol.1801530

Auffray, C., D. Fogg, M. Garfa, G. Elain, O. Join-Lambert, S. Kayal, S. Sarnacki, A. Cumano, G. Lauvau, and F. Geissmann. 2007. Monitoring of blood vessels and tissues by a population of monocytes with patrolling behavior. *Science*. 317:666–670. https://doi.org/10.1126/science.1142883

Becher, B., B.G. Durell, and R.J. Noelle. 2002. Experimental autoimmune encephalitis and inflammation in the absence of interleukin-12. *J. Clin. Invest.* 110:493–497. https://doi.org/10.1172/JCI15751

Beecham, A.H., N.A. Patsopoulos, D.K. Xifara, M.F. Davis, A. Kemppinen, C. Cotsapas, T.S. Shah, C. Spencer, D. Booth, A. Goris, et al. 2013. Analysis of immune-related loci identifies 48 new susceptibility variants for multiple sclerosis. *Nat. Genet.* 45:1353–1362. https://doi.org/10.1038/ng.2770

Bettelli, E., M. Pagany, H.L. Weiner, C. Linington, R.A. Sobel, and V.K. Kuchroo. 2003. Myelin oligodendrocyte glycoprotein-specific T cell receptor transgenic mice develop spontaneous autoimmune optic neuritis. *J. Exp. Med.* 197:1073–1081. https://doi.org/10.1084/JEM.20021603

Brightbill, H.D., E. Suto, N. Blaquiere, N. Ramamoorthi, S. Sujatha-Bhaskar, E.B. Gogol, G.M. Castanedo, B.T. Jackson, Y.C. Kwon, S. Haller, et al. 2018. NF-κB inducing kinase is a therapeutic target for systemic lupus erythematosus. *Nat. Commun.* 9:179. https://doi.org/10.1038/s41467-017-02672-0

Brockmann, L., A. Tran, Y. Huang, M. Edwards, C. Ronda, H.H. Wang, and I.I. Ivanov. 2023. Intestinal microbiota-specific Th17 cells possess regulatory properties and suppress effector T cells via c-MAF and IL-10. *Immunity*. 56:2719–2735.e7. https://doi.org/10.1016/J.IMMUNI.2023.11.003

Brown, C.C., H. Gudjonson, Y. Pritykin, D. Deep, V.P. Lavallée, A. Mendoza, R. Fromme, L. Mazutis, C. Ariyan, C. Leslie, et al. 2019. Transcriptional basis of mouse and human dendritic cell heterogeneity. *Cell*. 179:846–863.e24. https://doi.org/10.1016/j.cell.2019.09.035

Brunet, A., M. LeBel, B. Egarnes, C. Paquet-Bouchard, A.J. Lessard, J.P. Brown, and J. Gosselin. 2016. NR4A1-dependent Ly6Clow monocytes contribute to reducing joint inflammation in arthritic mice through Treg cells. *Eur. J. Immunol.* 46:2789–2800. https://doi.org/10.1002/eji.201646406

Caton, M.L., M.R. Smith-Raska, and B. Reizis. 2007. Notch-RBP-J signaling controls the homeostasis of CD8- dendritic cells in the spleen. *J. Exp. Med.* 204:1653–1664. https://doi.org/10.1084/jem.20062648

Cheng, J., X. Feng, Z. Li, F. Zhou, J.-M. Yang, and Y. Zhao. 2021. Pharmacological inhibition of NF-κB-inducing kinase (NIK) with small molecules for the treatment of human diseases. *RSC Med. Chem.* 12:552–565. https://doi.org/10.1039/d0md00361a

Chow, K.V., A.M. Lew, R.M. Sutherland, and Y. Zhan. 2016. Monocyte-derived dendritic cells promote Th polarization, whereas conventional dendritic cells promote Th proliferation. *J. Immunol.* 196:624–636. https://doi.org/10.4049/jimmunol.1501202

Croasdell, A., P.F. Duffney, N. Kim, S.H. Lacy, P.J. Sime, and R.P. Phipps. 2015. PPAR γ and the innate immune system mediate the resolution of inflammation. *PPAR Res.* 2015:1–20. https://doi.org/10.1155/2015/549691

Cua, D.J., J. Sherlock, Y. Chen, C.A. Murphy, B. Joyce, B. Seymour, L. Lucian, W. To, S. Kwan, T. Churakova, et al. 2003. Interleukin-23 rather

Downloaded from http://rupress.org/jem/article-pdf/223/4/e20242294/2027553/jem_20242294.pdf by guest on 31 May 2026

than interleukin-12 is the critical cytokine for autoimmune inflammation of the brain. *Nature*. 421:744–748. https://doi.org/10.1038/nature01355

Dann, E., N.C. Henderson, S.A. Teichmann, M.D. Morgan, and J.C. Marioni. 2022. Differential abundance testing on single-cell data using k-nearest neighbor graphs. *Nat. Biotechnol.* 40:245–253. https://doi.org/10.1038/s41587-021-01033-z

Egawa, M., K. Mukai, S. Yoshikawa, M. Iki, N. Mukaida, Y. Kawano, Y. Minegishi, and H. Karasuyama. 2013. Inflammatory monocytes recruited to allergic skin acquire an anti-inflammatory M2 phenotype via basophil-derived interleukin-4. *Immunity*. 38:570–580. https://doi.org/10.1016/j.immuni.2012.11.014

El-Behi, M., B. Ciric, H. Dai, Y. Yan, M. Cullimore, F. Safavi, G.X. Zhang, B.N. Dittel, and A. Rostami. 2011. The encephalitogenicity of TH 17 cells is dependent on IL-1- and IL-23-induced production of the cytokine GM-CSF. *Nat. Immunol.* 12:568–575. https://doi.org/10.1038/ni.2031

Giladi, A., L.K. Wagner, H. Li, D. Dörr, C. Medaglia, F. Paul, A. Shemer, S. Jung, S. Yona, M. Mack, et al. 2020. Cxcl10 + monocytes define a pathogenic subset in the central nervous system during autoimmune neuroinflammation. *Nat. Immunol.* 21:525–534. https://doi.org/10.1038/s41590-020-0661-1

Greter, M., J. Hofmann, and B. Becher. 2009. Neo-lymphoid aggregates in the adult liver can initiate potent cell-mediated immunity. *PLoS Biol.* 7: 1000109. https://doi.org/10.1371/journal.pbio.1000109

Hahn, M., A. Macht, A. Waisman, and N. Hövelmeyer. 2016. NF-κB-inducing kinase is essential for B-cell maintenance in mice. *Eur. J. Immunol.* 46: 732–741. https://doi.org/10.1002/eji.201546081

Hamdan, T.A., H. Bhat, L.B. Cham, T. Adomati, J. Lang, F. Li, A. Murtaza, C. Hardt, P.A. Lang, V. Duhan, and K.S. Lang. 2020. Map3k14 as a regulator of innate and adaptive immune response during acute viral infection. *Pathogens*. 9:96. https://doi.org/10.3390/pathogens9020096

Hao, Y., T. Stuart, M.H. Kowalski, S. Choudhary, P. Hoffman, A. Hartman, A. Srivastava, G. Molla, S. Madad, C. Fernandez-Granda, and R. Satija. 2023. Dictionary learning for integrative, multimodal and scalable single-cell analysis. *Nat. Biotechnol.* 42:293–304. https://doi.org/10.1038/s41587-023-01767-y

Hofmann, J., F. Mair, M. Greter, M. Schmidt-Supprian, and B. Becher. 2011. NIK signaling in dendritic cells but not in T cells is required for the development of effector T cells and cell-mediated immune responses. *J. Exp. Med.* 208:1917–1929. https://doi.org/10.1084/jem.20110128

Huang, T., Z. Gao, Y. Zhang, K. Fan, F. Wang, Y. Li, J. Zhong, H.Y. Fan, Q. Cao, J. Zhou, et al. 2018. CRL4DCAF2 negatively regulates IL-23 production in dendritic cells and limits the development of psoriasis. *J. Exp. Med.* 215: 1999–2017. https://doi.org/10.1084/jem.20180210

Hussman, J.P., A.H. Beecham, M. Schmidt, E.R. Martin, J.L. McCauley, J.M. Vance, J.L. Haines, and M.A. Pericak-Vance. 2016. GWAS analysis implicates NF-κB-mediated induction of inflammatory T cells in multiple sclerosis. *Genes Immun.* 17:305–312. https://doi.org/10.1038/gene.2016.23

Isaksson, M., B.A. Lundgren, K.M. Ahlgren, O. Kämpe, and A. Lobell. 2012. Conditional DC depletion does not affect priming of encephalitogenic Th cells in EAE. *Eur. J. Immunol.* 42:2555–2563. https://doi.org/10.1002/eji.201142239

Jakubzick, C.V., G.J. Randolph, and P.M. Henson. 2017. Monocyte differentiation and antigen-presenting functions. *Nat. Rev. Immunol.* 17:349–362. https://doi.org/10.1038/nri.2017.28

Jie, Z., C.-J. Ko, H. Wang, X. Xie, Y. Li, M. Gu, L. Zhu, J.-Y. Yang, T. Gao, W. Ru, et al. 2021. Microglia promote autoimmune inflammation via the non-canonical NF-κB pathway. *Sci. Adv.* 7:eabh0609. https://doi.org/10.1126/sciadv.abh0609

Jie, Z., J.Y. Yang, M. Gu, H. Wang, X. Xie, Y. Li, T. Liu, L. Zhu, J. Shi, L. Zhang, et al. 2018. NIK signaling axis regulates dendritic cell function in intestinal immunity and homeostasis. *Nat. Immunol.* 19:1224–1235. https://doi.org/10.1038/s41590-018-0206-z

Jin, W., X.-F. Zhou, J. Yu, X. Cheng, and S.-C. Sun. 2009. Regulation of Th17 cell differentiation and EAE induction by MAP3K NIK. *Blood*. 113: 6603–6610. https://doi.org/10.1182/blood-2008-12-192914

Jung, S., J. Aliberti, P. Graemmel, M.J. Sunshine, G.W. Kreutzberg, A. Sher, and D.R. Littman. 2000. Analysis of fractalkine receptor CX 3 CR1 function by targeted deletion and green fluorescent protein reporter gene insertion. *Mol. Cell Biol.* 20:4106–4114. https://doi.org/10.1128/mcb.20.11.4106-4114.2000

Kalinski, A.L., C. Yoon, L.D. Huffman, P.C. Duncker, R. Kohen, R. Passino, H. Hafner, C. Johnson, R. Kawaguchi, K.S. Carbajal, et al. 2020. Analysis of the immune response to sciatic nerve injury identifies efferocytosis as a key mechanism of nerve debridement. *Elife*. 9:1–41. https://doi.org/10.7554/ELIFE.60223

Katakam, A.K., H. Brightbill, C. Franci, C. Kung, V. Nunez, C. Jones, I. Peng, S. Jeet, L.C. Wu, I. Mellman, et al. 2015. Dendritic cells require NIK for CD40-dependent cross-priming of CD8+ T cells. *Proc. Natl. Acad. Sci. USA*. 112:14664–14669. https://doi.org/10.1073/pnas.1520627112

Keeney, J.N., A.D. Winters, R. Sitcheran, and A.P. West. 2023. NF-κB-Inducing kinase governs the mitochondrial respiratory capacity, differentiation, and inflammatory status of innate immune cells. *J Immunol.* 210:1123–1133. https://doi.org/10.4049/jimmunol.2200596

Lacher, S.M., C. Thurm, U. Distler, A.N. Mohebiany, N. Israel, M. Kitic, A. Ebering, Y. Tang, M. Klein, G.H. Wabnitz, et al. 2018. NF-κB inducing kinase (NIK) is an essential post-transcriptional regulator of T-cell activation affecting F-actin dynamics and TCR signaling. *J. Autoimmun.* 94: 110–121. https://doi.org/10.1016/j.jaut.2018.07.017

Leylek, R., M. Alcántara-Hernández, Z. Lanzar, A. Lüdtke, O.A. Perez, B. Reizis, and J. Idoyaga. 2019. Integrated cross-species analysis identifies a conserved transitional dendritic cell population. *Cell Rep.* 29:3736–3750.e8. https://doi.org/10.1016/j.celrep.2019.11.042

Liao, G., M. Zhang, E.W. Harhaj, and S.-C. Sun. 2004. Regulation of the NF-kappaB-inducing kinase by tumor necrosis factor receptor-associated factor 3-induced degradation. *J. Biol. Chem.* 279:26243–26250. https://doi.org/10.1074/jbc.M403286200

Li, M.Y., L.C. Chong, B.W. Woolcock, A. Telenius, S. Ben-Neriah, G.W. Slack, V. Lam, A. Jiang, E. Viganò, T. Aoki, et al. 2022a. TRAF3 loss-of-function reveals the non-canonical NF-Kb pathway as a therapeutic target in diffuse large B-cell lymphoma. *Blood*. 140:2042–2043. https://doi.org/10.1182/blood-2022-159679

Li, Y.H., Y. Zhang, G. Pan, L.X. Xiang, D.C. Luo, and J.Z. Shao. 2022b. Occurrences and functions of Ly6Chi and Ly6Clo macrophages in health and disease. *Front. Immunol.* 13:901672. https://doi.org/10.3389/fimmu.2022.901672

Luche, H., O. Weber, T.N. Rao, C. Blum, and H.J. Fehling. 2007. Faithful activation of an extra-bright red fluorescent protein in "knock-in" Cre-reporter mice ideally suited for lineage tracing studies. *Eur. J. Immunol.* 37:43–53. https://doi.org/10.1002/EJI.200636745

Lukowski, S.W., I. Rødahl, S. Kelly, M. Yu, J. Gotley, C. Zhou, S. Millard, S.B. Andersen, A.N. Christ, G. Belz, et al. 2021. Absence of Batf3 reveals a new dimension of cell state heterogeneity within conventional dendritic cells. *iScience*. 24:102402. https://doi.org/10.1016/j.isci.2021.102402

Luu, T., J.F. Cheung, J. Baccon, and H. Waldner. 2021. Priming of myelin-specific T cells in the absence of dendritic cells results in accelerated development of experimental autoimmune. *PLoS One*. 16:e0250340. https://doi.org/10.1371/journal.pone.0250340

Miyake, K., J. Ito, K. Takahashi, J. Nakabayashi, F. Brombacher, S. Shichino, S. Yoshikawa, S. Miyake, and H. Karasuyama. 2024. Single-cell transcriptomics identifies the differentiation trajectory from inflammatory monocytes to pro-resolving macrophages in a mouse skin allergy model. *Nat. Commun.* 15:1666. https://doi.org/10.1038/s41467-024-46148-4

Miyawaki, S., Y. Nakamura, H. Suzuka, M. Koba, Y. Shibata, R. Yasumizu, and S. Ikehara. 1994. A new mutation, aly, that induces a generalized lack of lymph nodes accompanied by immunodeficiency in mice. *Eur. J. Immunol.* 24:429–434. https://doi.org/10.1002/eji.1830240224

Nowicka, M., C. Krieg, H.L. Crowell, L.M. Weber, F.J. Hartmann, S. Guglietta, B. Becher, M.P. Levesque, and M.D. Robinson. 2019. CyTOF workflow: Differential discovery in high-throughput high-dimensional cytometry datasets. *F1000Res.* 6:748. https://doi.org/10.12688/f1000research.11622.4

Pflug, K.M., and R. Sitcheran. 2020. Targeting NF-κB-inducing kinase (NIK) in immunity, inflammation, and cancer. *Int. J. Mol. Sci.* 21:1–19. https://doi.org/10.3390/ijms21228470

Regen, T., S. Isaac, A. Amorim, N.G. Núñez, J. Hauptmann, A. Shanmugavadivu, M. Klein, R. Sankowski, I.A. Mufazalov, N. Yogev, et al. 2021. IL-17 controls central nervous system autoimmunity through the intestinal microbiome. *Sci. Immunol.* 6:eaaz6563. https://doi.org/10.1126/SCIIMMUNOL.AAZ6563;CTYPE:STRING

Sage, P.T., F.A. Schildberg, R.A. Sobel, V.K. Kuchroo, G.J. Freeman, and A.H. Sharpe. 2018. Dendritic cell PD-L1 limits autoimmunity and follicular T cell differentiation and function. *J. Immunol.* 200:2592–2602. https://doi.org/10.4049/jimmunol.1701231

Schlechter, N., B. Glanzmann, E.G. Hoal, M. Schoeman, B.S. Petersen, A. Franke, Y.L. Lau, M. Urban, P.D. van Helden, M.M. Esser, et al. 2017. Exome sequencing identifies a novel MAP3K14 mutation in recessive atypical combined immunodeficiency. *Front. Immunol.* 8:1624. https://doi.org/10.3389/fimmu.2017.01624

Downloaded from http://rupress.org/jem/article-pdf/223/4/e20242294/2027553/jem_20242294.pdf by guest on 31 May 2026

Sha, H., D. Zhang, Y. Zhang, Y. Wen, and Y. Wang. 2017. ATF3 promotes migration and M1/M2 polarization of macrophages by activating tenascin-C via Wnt/β-catenin pathway. *Mol. Med. Rep.* 16:3641–3647. https://doi.org/10.3892/mmr.2017.6992

Shih, R.-H., C.-Y. Wang, and C.-M. Yang. 2015. NF-kappaB signaling pathways in neurological inflammation: A mini review. *Front. Mol. Neurosci.* 8:77. https://doi.org/10.3389/fnmol.2015.00077

Sun, S.-C. 2012. The noncanonical NF-κB pathway. *Immunol. Rev.* 246: 125–140. https://doi.org/10.1111/j.1600-065X.2011.01088.x

Sun, S.C. 2017. The non-canonical NF-κB pathway in immunity and inflammation. *Nat. Rev. Immunol.* 17:545–558. https://doi.org/10.1038/nri.2017.52

Sun, S.-C., and S.C. Ley. 2008. New insights into NF-kappaB regulation and function. *Trends Immunol.* 29:469–478. https://doi.org/10.1016/j.it.2008.07.003

Termeer, C., M. Averbeck, H. Hara, H. Eibel, P. Herrlich, J. Sleeman, and J.C. Simon. 2003. Targeting dendritic cells with CD44 monoclonal antibodies selectively inhibits the proliferation of naive CD4+ T-helper cells by induction of FAS-independent T-cell apoptosis. *Immunology*. 109: 32–40. https://doi.org/10.1046/j.1365-2567.2003.01617.x

Vaknin-dembinsky, A., K. Balashov, and H.L. Weiner. 2006. IL-23 is increased in dendritic cells in multiple sclerosis and down-regulation of IL-23 by antisense oligos increases dendritic cell IL-10 production. *J. Immunol.* 176:7768–7774. https://doi.org/10.4049/jimmunol.176.12.7768

Waisman, A., D. Lukas, B.E. Clausen, and N. Yogev. 2017. Dendritic cells as gatekeepers of tolerance. *Semin. Immunopathol.* 39:153–163. https://doi.org/10.1007/s00281-016-0583-z

Weiss, J.M., J. Sleeman, A.C. Renkl, H. Dittmar, C.C. Termeer, S. Taxis, N. Howells, M. Hofmann, G. Köhler, E. Schöpf, et al. 1997. An essential role for CD44 variant isoforms in epidermal langerhans cell and blood dendritic cell function. *J. Cell Biol.* 137:1137–1147. https://doi.org/10.1083/jcb.137.5.1137

Willmann, K.L., S. Klaver, F. Do U, E. Santos-Valente, W. Garncarz, I. Bilic, E. Mace, E. Salzer, C. Domínguez Conde, H. Sic, et al. 2014. Biallelic loss-of-function mutation in NIK causes a primary immunodeficiency with multifaceted aberrant lymphoid immunity. *Nat. Commun.* 5: 5360. https://doi.org/10.1038/ncomms6360

Wolf, Y., S. Yona, K.W. Kim, and S. Jung. 2013. Microglia, seen from the CX3CR1 angle. *Front. Cell Neurosci.* 7:26. https://doi.org/10.3389/fncel.2013.00026

Wu, T., E. Hu, S. Xu, M. Chen, P. Guo, Z. Dai, T. Feng, L. Zhou, W. Tang, L. Zhan, et al. 2021. clusterProfiler 4.0: A universal enrichment tool for interpreting omics data. *Innovation*. 2:100141. https://doi.org/10.1016/j.xinn.2021.100141

Xiao, G., E.W. Harhaj, and S.C. Sun. 2001. NF-κB-inducing kinase regulates the processing of NF-κB2 p100. *Mol. Cell*. 7:401–409. https://doi.org/10.1016/S1097-2765(01)00187-3

Yogev, N., F. Frommer, D. Lukas, K. Kautz-Neu, K. Karram, D. Ielo, E. von Stebut, H.C. Probst, M. van den Broek, D. Riethmacher, et al. 2012. Dendritic cells ameliorate autoimmunity in the CNS by controlling the homeostasis of PD-1 receptor+ regulatory T cells. *Immunity*. 37:264–275. https://doi.org/10.1016/j.immuni.2012.05.025

Yona, S., K.W. Kim, Y. Wolf, A. Mildner, D. Varol, M. Breker, D. Strauss-Ayali, S. Viukov, M. Guilliams, A. Misharin, et al. 2013. Fate mapping reveals origins and dynamics of monocytes and tissue macrophages under homeostasis. *Immunity*. 38:79–91. https://doi.org/10.1016/j.immuni.2012.12.001

Zhang, N., S. Shen, M. Yang, S. He, C. Liu, H. Li, T. Lu, H. Liu, Q. Hu, W. Tang, and Y. Chen. 2024. Design, synthesis, and biological evaluation of a novel NIK inhibitor with anti-inflammatory and hepatoprotective effects for sepsis treatment. *J. Med. Chem.* 67:5617–5641. https://doi.org/10.1021/acs.jmedchem.3c02266

Downloaded from http://rupress.org/jem/article-pdf/223/4/e20242294/2027553/jem_20242294.pdf by guest on 31 May 2026

JEM

Supplemental material

Downloaded from http://rupress.org/jem/article-pdf/223/4/e20242294/2027553/jem_20242294.pdf by guest on 31 May 2026

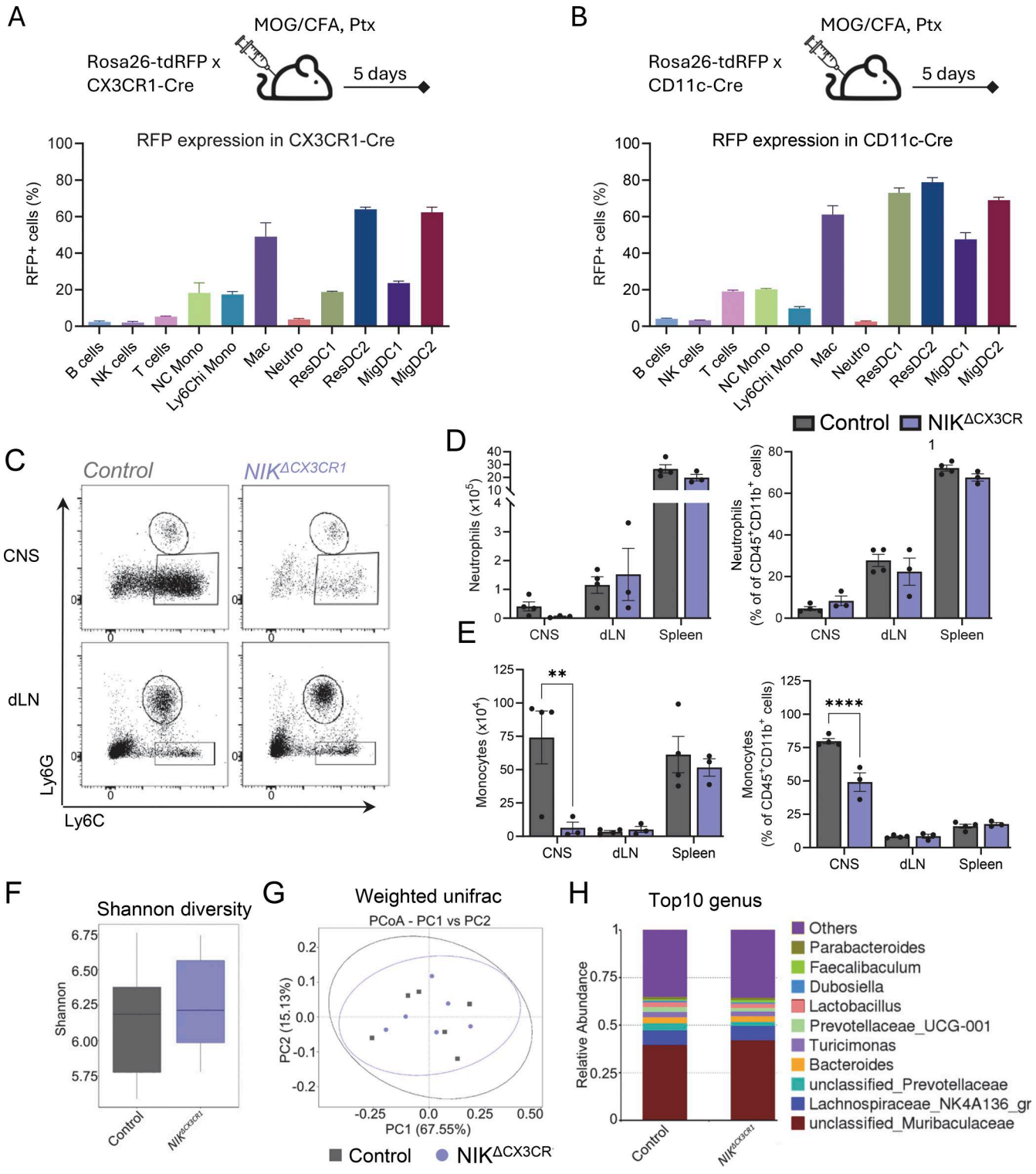

Figure S1. **Neutrophils and monocytes at the peak of EAE. (A and B)** Percentage of RFP-expressing cells in different populations in the RFP CX3CR1-Cre and (B) RFP CD11c-Cre in the dLNs 5 days after MOG immunization. **(C)** Gating for Ly6G$^+$ neutrophils and Ly6C$^+$ monocytes in the CNS and dLN, gated on CD11b$^+$/live/single cells. **(D and E)** Cell number and percentages of neutrophils and (E) monocytes in the CNS, dLN, and spleen. **(F–H)** α-Diversity (Shannon index) of fecal microbiota from naïve control and NIKΔCX3CR1 mice housed under identical SPF conditions. **(G)** β-Diversity analysis visualized by weighted UniFrac PCoA. **(H)** Relative abundance of dominant bacterial taxa at the genus level. Data in A, B, D, and E are shown as the mean ± SEM and analyzed using two-way ANOVA with Šídák's multiple comparisons test. **P < 0.01, ****P < 0.0001. Each dot represents one mouse. Data are from three independent experiments. PCoA, principal coordinates analysis.

Downloaded from http://rupress.org/jem/article-pdf/223/4/e20242294/2027553/jem_20242294.pdf by guest on 31 May 2026

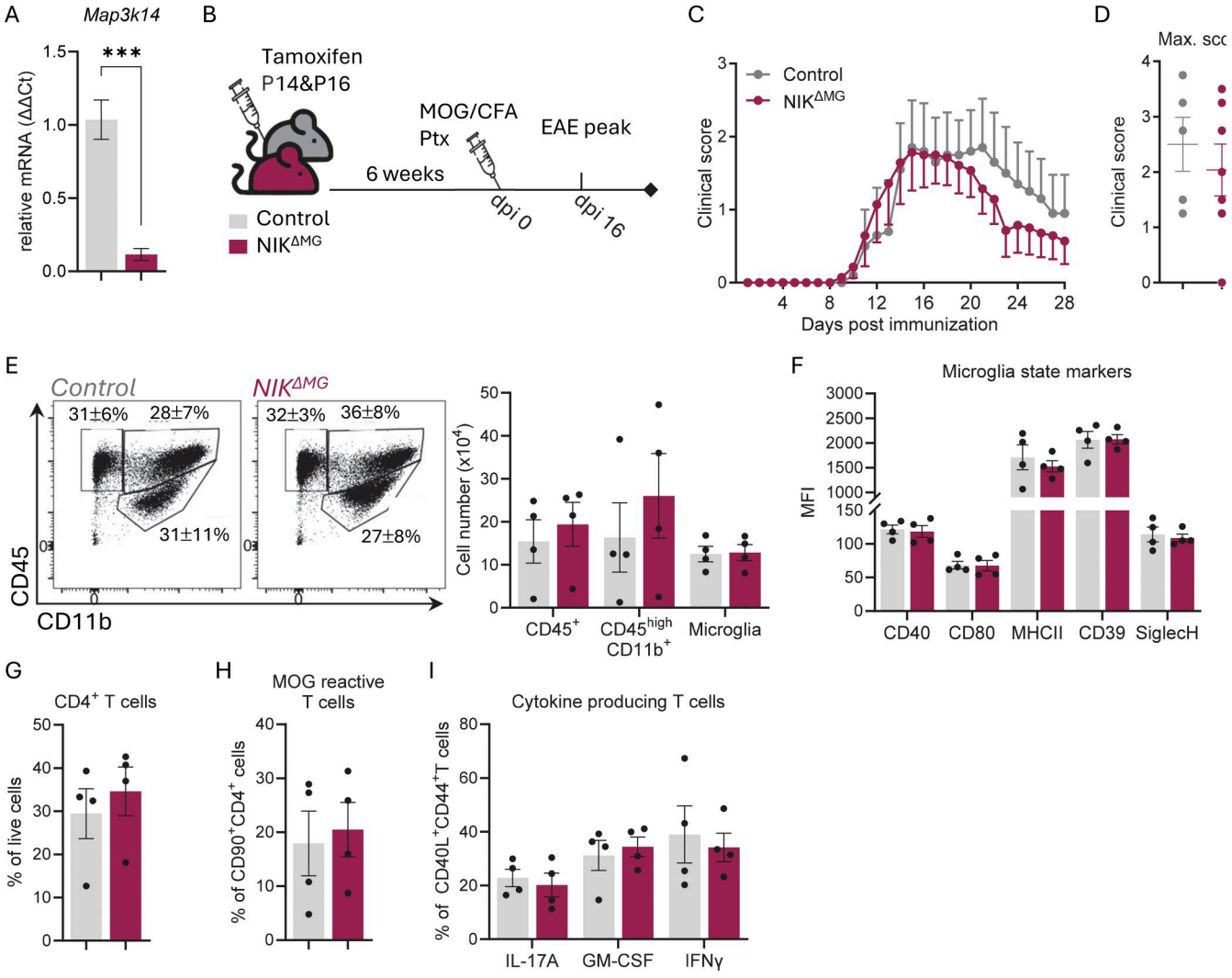

Figure S2. **NIK in microglia does not play a role in EAE disease development. (A)** Fold change in Map3k14 (NIK) expression relative to the control, calculated using the ΔΔCT method. Expression was measured in isolated microglia ($CD11b^+$ cells from the brain) 10 wk after tamoxifen administration. **(C)** Disease course of $NIK^{\Delta MG}$ and littermate controls. **(B)** Mice were injected with tamoxifen at 2 wk of age to induce the deletion of NIK in $CX3CR1^+$ cells. After 6 wk, mice were immunized with MOG_{35-55}/CFA and PTx. **(D)** Maximum EAE score. **(E)** Representative flow cytometry plots and the number of microglia ($CD11b^+CD45^{int}$), infiltrating $CD45^{high}$ and $CD11b^+CD45^{high}$ immune cells into the CNS (brain and spinal cord) during the peak of EAE (16 dpi). **(F)** MFI of different activation markers on microglia. **(G–I)** Percentages of infiltrating $CD4^+CD90^+$ T cells, (H) MOG-responding $CD40L^+CD44^+$ T cells, and (I) cytokine-producing T cells into the CNS, after being subjected to a MOG_{35-55} antigen recall assay. Data in graphs are shown as the mean ± SEM and analyzed using two-tailed unpaired Student's *t* test or two-way ANOVA with Šídák's multiple comparisons test. ***P < 0.001. dpi = days after immunization. Each dot represents one mouse. Data are from three independent experiments. MFI, median fluorescence intensity.

Downloaded from http://rupress.org/jem/article-pdf/223/4/e20242294/2027553/jem_20242294.pdf by guest on 31 May 2026

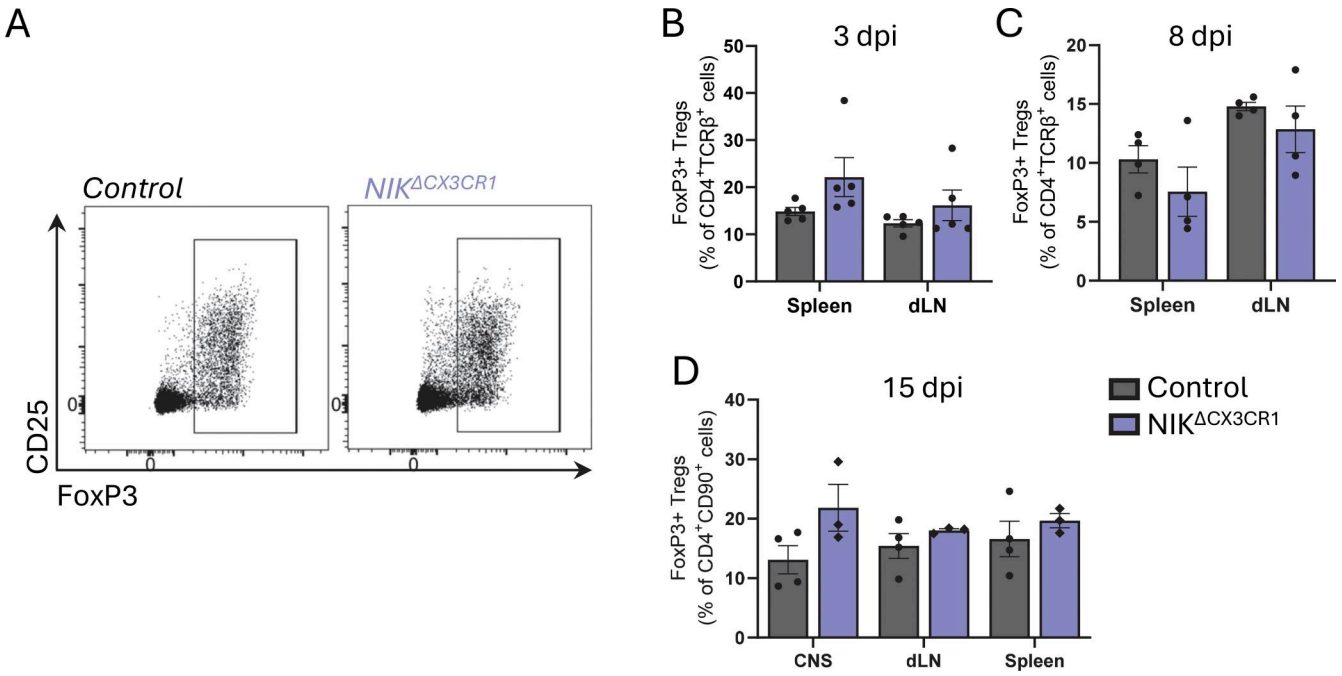

Figure S3. **No differences in the percentage of T_{regs} after MOG immunization. (A–C)** Example of the gating for FoxP3$^+$ T_{regs} in the dLN at 8 dpi with $MOG_{35–55}$/CFA and PTx. The percentages of T_{regs} in the (B) spleen and dLNs at 3 dpi and (C) 8 dpi. **(D)** Percentages of T_{regs} in the CNS, dLN, and spleen during the peak of EAE. T_{regs} were pregated on CD45$^+$, TCRβ$^+$ or CD90$^+$, and CD4$^+$ cells; dead cells and duplets were excluded. Data in graphs are shown as the mean ± SEM and analyzed using two-way ANOVA with Šídák's multiple comparisons test. dpi = days after immunization. Each dot represents one mouse. Data are from three independent experiments.

Downloaded from http://rupress.org/jem/article-pdf/223/4/e20242294/2027553/jem_20242294.pdf by guest on 31 May 2026

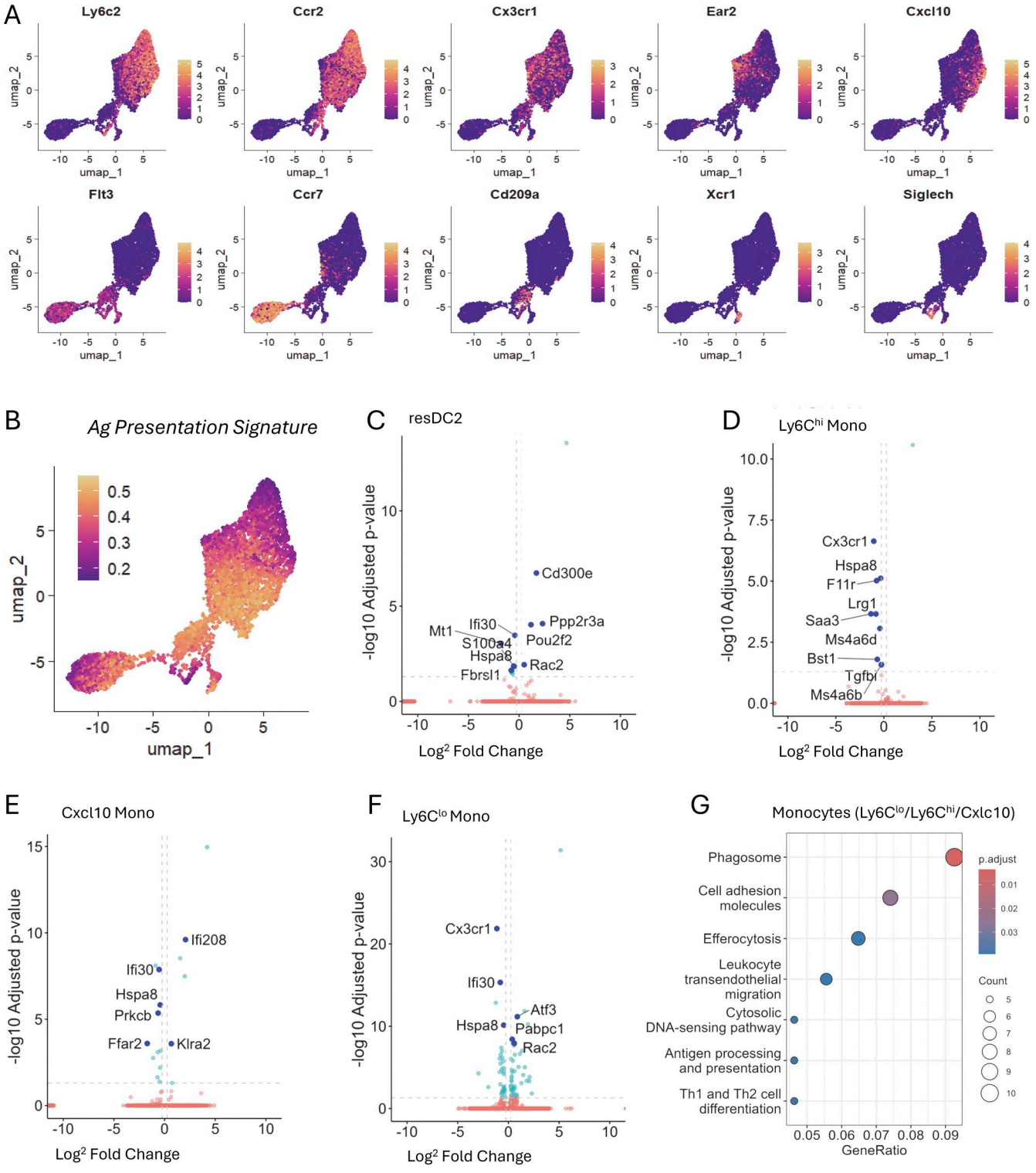

Figure S4. **scRNA-seq. (A)** UMAP displaying the expression of different cell markers to identify cell types. **(B)** Antigen presentation signature projected on the UMAP. **(C–F)** Volcano plot of DEGs between NIK$^{\Delta CX3CR1}$ (n = 4) and control (n = 4) in the resDC2 subset, (D) Ly6C^{hi} monocyte subset, (E) Cxcl10 monocyte subset, and (F) Ly6C^{lo} monocyte subset. Left are genes downregulated in NIK$^{\Delta CX3CR1}$, and right are genes upregulated in NIK$^{\Delta CX3CR1}$. Genes on the X or Y chromosome, ribosomal genes, and low-reproducibility genes were excluded from labels. **(G)** KEGG pathway enrichment analysis was performed on DEGs (adjusted P < 0.05 and $|\log_2$ fold change$|$ >0.1 and less than −0.1) from the combined monocyte clusters (Ly6C^{hi}/Ly6C^{lo}/Cxcl10). The dot plot shows enriched pathways ranked by significance. Each dot represents a KEGG pathway. Circle size = count of DEGs found within each pathway; color = adjusted P value.

Downloaded from http://rupress.org/jem/article-pdf/223/4/e20242294/2027553/jem_20242294.pdf by guest on 31 May 2026

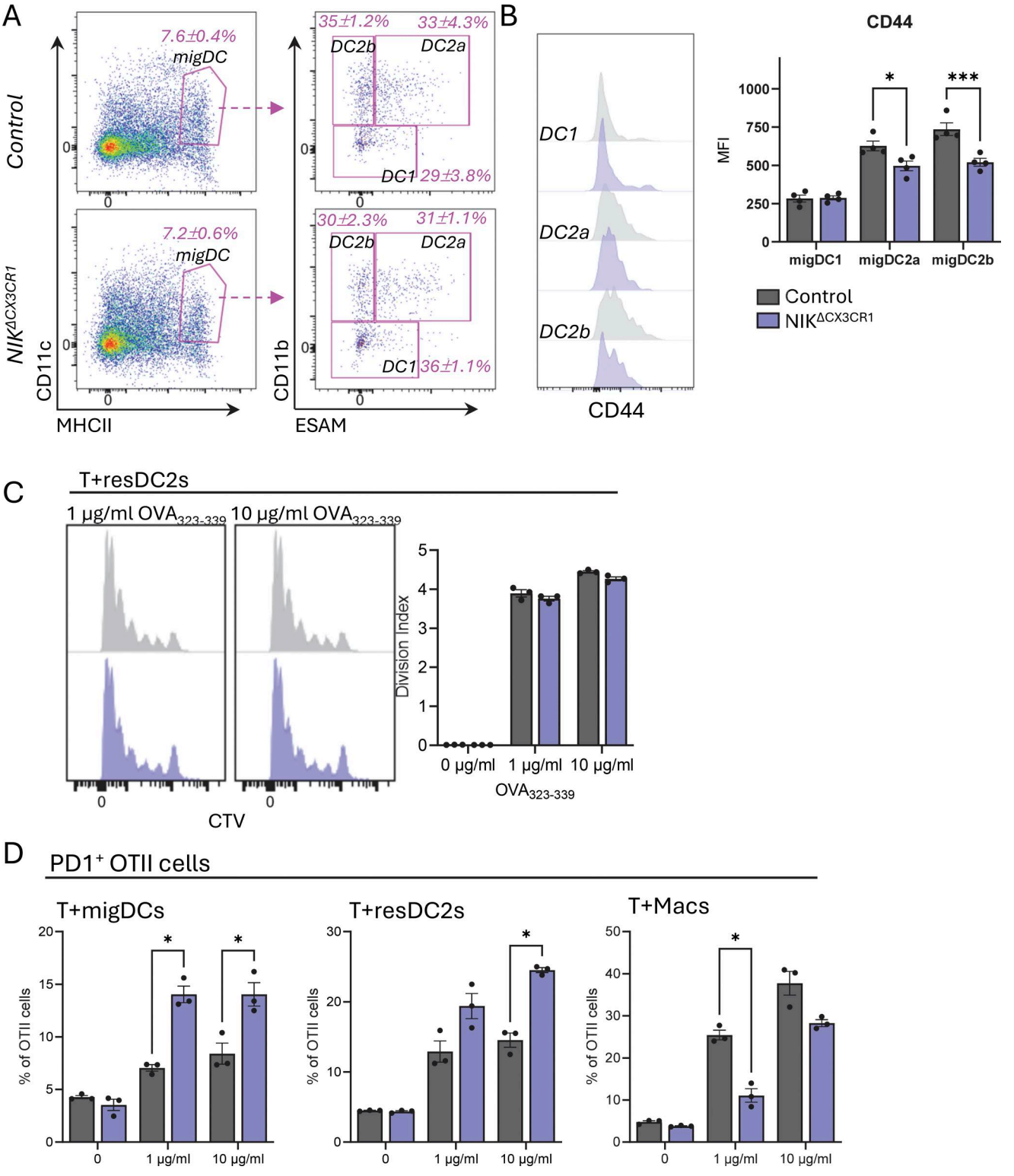

Figure S5. **Reduced CD44 on myeloid populations during early priming in the dLNs. (A)** Gating strategy of MHCII^{high}CD11c^{int} migDCs, which were gated further for CD11b^{+}ESAM^{-} migDC2b, CD11b^{+}ESAM^{+} migDC2a, and CD11b-migDC1 in the dLNs 3 days after MOG$_{35-55}$ immunization. The mean percentage and SEM are shown in pink for each cluster (n = 4 per group). Doublets, dead cells, CD3+/CD19+ cells, eosinophils, and neutrophils were excluded. **(B)** Histogram and the MFI of CD44 expression on migDC1, migDC2a, and migDC2b. **(C)** Representative flow cytometry histograms showing CTV dilution of OT-II CD4^{+} T cells cocultured with resident DC2s (T + resDC2s) from dLNs from control or NIK$^{\Delta CX3CR1}$ mice. Cells were pulsed with the indicated concentrations of OVA$_{323-339}$ peptide for 1 h prior to coculture. Division index of OT-II T cells, reflecting the average number of divisions per input cell. **(D)** Percentage of PD1+ OT-II cells from the antigen presentation assay. Data in B, C, and D are shown as the mean ± SEM and analyzed using two-way ANOVA with Šídák's multiple comparisons test. *P < 0.05, ***P < 0.001. Each dot represents one mouse. Data are from at least two independent experiments. MFI, median fluorescence intensity; CTV, CellTrace Violet.

Downloaded from http://rupress.org/jem/article-pdf/223/4/e20242294/2027553/jem_20242294.pdf by guest on 31 May 2026

Provided online is Table S1. Table S1 shows the DEGs for each cluster and KEGG results of the scRNA-seq data.

Downloaded from http://rupress.org/jem/article-pdf/223/4/e20242294/2027553/jem_20242294.pdf by guest on 31 May 2026